Photophysical and Redox Properties of Degenerately Doped Nanocrystals

Jose Juan Araujo

A dissertation

submitted in partial fulfillment of the

requirements for the degree of

Doctor of Philosophy

University of Washington

2020

Reading Committee:

Daniel R. Gamelin, Chair

Brandi M. Cossairt

Cody W. Schlenker

Program Authorized to Offer Degree:

Chemistry

University of Washington

Abstract

Photophysical and Redox Properties of Degenerately Doped Nanocrystals

Jose Juan Araujo

Chair of the Supervisory Committee:
Professor Daniel R. Gamelin
Department of Chemistry

For the past few decades, semiconductor nanocrystals (NCs) have been the subject of intense interdisciplinary research in both fundamental science and device engineering. Their size-tunable electronic and optical properties, solution processability, and diverse synthetic chemistries make them attractive candidates for applications such as photovoltaics, photocatalysis, and lighting technologies. Besides the well-known quantum confinement effect, the introduction of dopants introduces many more opportunities to tune the electronic, optical, and magnetic properties of NCs. This thesis focuses on NCs containing excess band-like electrons, their photophysical properties, and the redox chemistries associated with these dopants in relation to their charge-compensation mechanisms.

Chapter 1 outlines the basic properties of degenerately doped NCs. Methods for preparing degenerately doped NCs are discussed, along with spectroscopic and electrochemical techniques for studying their optical and electronic properties. Chapter 2 describes a new method for preparing photodoped PbSe quantum dots with high electron densities. These high doping densities allow for a careful analysis of the changes in electronic absorption, which reveal conclusive evidence for the assignment of the electronic transitions in their absorption spectra. Chapter 3 employs spectroelectrochemical potentiometry to study the redox properties of excess electrons in Sn^{4+}:In_2O_3 NCs. An important difference is observed between the redox properties of electrons added by photodoping compared to aliovalent doping. These differences reflect the impact of the charge-compensation motif on determining the stability of charges in degenerately doped NCs.

TABLE OF CONTENTS

LIST OF FIGURES

LIST OF SCHEMES

LIST OF TABLES

Chapter 1. Introduction

1.1 Overview

Semiconductor nanocrystals (NCs) draw a tremendous amount of research effort by academic and industrial researchers worldwide. With physical and electronic properties that lie between molecules and bulk, these materials have enabled exciting innovations in fundamental science and technology.[1-5] Electronically doped NCs, like their bulk analogs, offer additional tunability of redox and various photophysical properties, increasing their feasibility as candidates for device applications and enabling the study of new electronic properties.[6] Therefore, the preparation of degenerately doped NCs and a complete understanding of their electronic properties is required to progress the fundamental understanding of these materials and inform the rational design of NC-based devices. This chapter introduces the basic properties of degenerately doped NCs and experimental methods for studying them. First, the spectroscopic features that are manifested in degenerately doped NCs are discussed, with a focus on electronic absorption spectra. Four methods for preparing degenerately doped nanocrystals are described. Next, spectroelectrochemical potentiometry is highlighted as a means for direct measurement of the redox properties of colloidal NCs. Finally, the redox properties of excess charges are discussed in terms of charge-compensation either at the surface or within the NC lattice.

1.2 Degenerately Doped Semiconductors

Semiconductors are an important class of materials with optical and electronic properties that enable many electronics applications. These materials have a conduction band (CB) and valence band (VB) that are separated by an energetic barrier (bandgap, E_g). In most cases, electrons

can be excited from the VB to the CB by light with energy greater than E_g, creating an electron-hole pair (exciton). Excitons can recombine non-radiatively or radiatively to emit light with energy $h\nu = E_g$, or the charges can be separated to collect current.

Semiconductors conductivity can be tuned through electronic doping, which changes the Fermi level (E_F) relative to the bands. The Fermi level is the potential at which there is a 50% probability of finding an electron within the electronic structure of a material. For intrinsic semiconductors (and insulators), E_F is in the middle of the bandgap where there are no electronic states, leading to low conductivity. The addition of electron density (*n*-type doping) or hole density (*p*-type doping) to the CB or VB, respectively, moves the Fermi level into the bands, turning on metallic-like conductivity. These scenarios are depicted below in Scheme 1.1. This Fermi level tunability is necessary for the development of devices such as transistors, photovoltaics, and light-emitting diodes. The development of electronic doping techniques for NCs is therefore necessary if similar advancements are to be achieved at the nanoscale.

Scheme 1.1. Fermi level for intrinsic, *n*-type doped, and *p*-type doped semiconductors

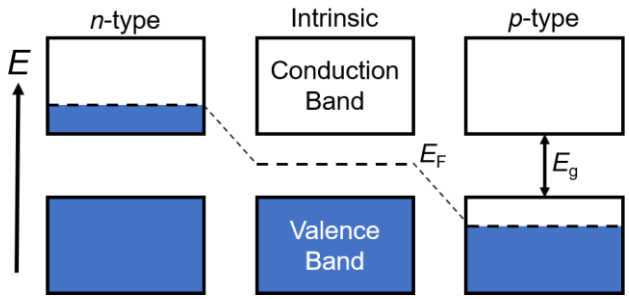

1.3 **Degenerately Doped Nanocrystals**

Nanocrystals have many attractive properties that are not present in their bulk analogs. NCs are most typically synthesized as colloids, allowing for solution processing and ease of high-

quality spectroscopic measurements. Their radii are often smaller than the Bohr exciton radius, turning on size-tunable quantum confinement effects that changes absorption, emission, and electronic properties.

Electronic doping is a useful way to perturb the optical and electronic properties of NCs. Changes in redox properties,[7] carrier recombination dynamics,[8-10] and electronic absorption[11-12] of degenerately doped NCs provide valuable insight into fundamental properties that cannot be studied in intrinsic (*i.e.* non-electronically doped) NCs. Because nanocrystals are electronically different from their bulk analogs, it is critical to understand their properties before new scientific developments and applications are developed.

1.4 **Spectroscopic Signatures of Degenerately Doped Nanocrystals**

Optical absorption measurements are highly diagnostic of the presence of excess charge carriers in NCs. Here, *n*-type doping is discussed as an example, but the same spectroscopic features apply to *p*-type doping. As the CB becomes populated with electrons (*i.e.* becomes *n*-type), subsequent electronic *interband* transitions (*i.e.*, transitions between the VB and CB) lose intensity due to Pauli blocking,[13] resulting in a bleach of the bandgap-edge absorption feature. Meanwhile, these CB electrons can undergo new *intraband* transitions (*i.e.*, transitions within the band) to higher energy levels within the CB. These transitions are much lower in energy than the interband transitions and are typically located in the NIR to MIR region.[14-19] These absorption features are exemplified in Figure 1.1, demonstrating the excitonic bleach at ~2.1 eV and the NIR absorption at ~0.3 eV as electrons are added to the CB of CdSe NCs.[15] Heavily doped NCs ($> 10^{20}$ cm^{-3}) exhibit broad NIR absorption attributed to localized surface plasmon resonance (LSPR). In

this case, the LSPR absorption feature is not due solely to discreet intraband transitions, but rather to the collective oscillation of all excess charge carriers at some resonant frequency.[3,20]

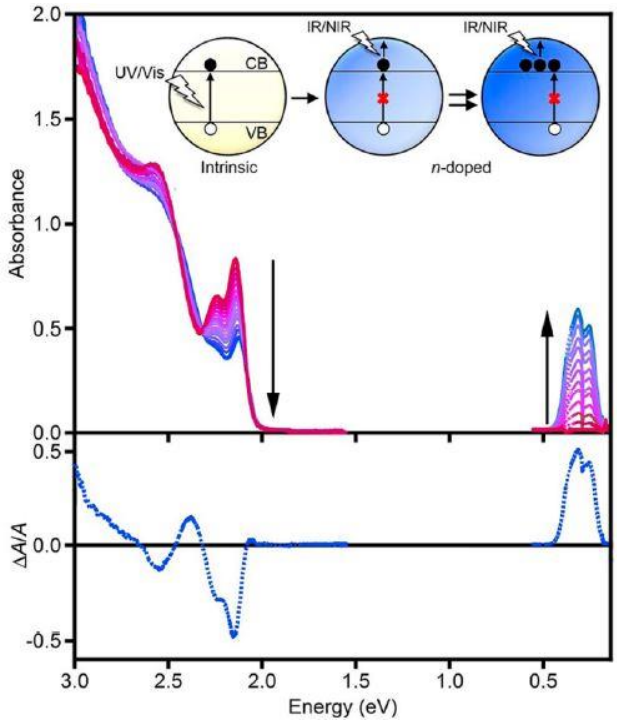

Figure 1.1. (Top) Absorption spectra of CdSe NCs at various stages of photodoping. The excitonic absorption feature at ~2.1 eV loses intensity and redshifts as electrons are added to the CB. Concurrently, a new NIR absorption feature grows in at ~0.3 eV. (Bottom) Differential absorption spectra. The inset shows a schematic representation of the photodoping mechanism. Reprinted with permission from ref.[6] Copyright 2015 American Chemical Society.

The excitonic absorption bleach is also accompanied by a shift in the peak position. Quantum-confined NCs, such as CdSe and PbSe, exhibit redshifts (often referred to as a Stark shift) of their excitonic absorption peaks as electrons are added to the CB.[9,11,15] This behavior, which is also observed in NCs containing multiple excitons, is attributed to a rearrangement of the excitonic wavefunctions that minimizes coulombic repulsion between the exciton and excess charges. As a result, the overlap between the electron and hole wavefunctions decreases, which decreases the energy of the excitonic transition.[11] Nanocrystals that are not quantum confined, such as large ZnO and In_2O_3, exhibit blueshifts of their bandgap absorption.[21-22] In this case, as the

CB becomes filled, the lowest energy electronic transition is no longer to the edge of the CB, but to a higher energy state within the band. This behavior is known as the Burstein-Moss shift.

An important aspect about degenerately doped NCs is that their absorption spectra are a quantitative measure of the average number of CB electrons ($\langle n \rangle$) or VB holes ($\langle p \rangle$) per NC. For quantum confined NCs such as CdSe and PbSe, $\langle n \rangle$ is simply given by the relation $\langle n \rangle = \left| \Delta A/A_0 \right| \times \delta$, where $\left| \Delta A/A_0 \right|$ is the normalized differential absorbance at the exciton and δ is the degeneracy of the CB edge.[15,19,23-24] The CB edge can accommodate δ electrons, therefore population of the CB blocks subsequent excitonic transitions by $\langle n \rangle/\delta$. For example, a $\left| \Delta A/A_0 \right|$ value of 0.5 for CdSe NCs corresponds to $\langle n \rangle = 1$ ($\delta = 2$), and a $\left| \Delta A/A_0 \right|$ value of 0.75 for PbSe NCs corresponds to $\langle n \rangle = 6$ ($\delta = 8$).

Heavily doped NCs exhibiting LSPR absorption, such as photodoped ZnO, AZO, photodoped In_2O_3, ITO, and $Cu_{2-x}E$ (E = S, Se) are often analyzed using the Drude model.[2-3,20,25-29] This analysis uses spectral fitting to extract dopant densities, but it relies on using bulk parameters, such as effective mass, that may be different in NCs. Alternatively, $\langle n \rangle$ can be measured directly by quantitative titrations.[21-22,25] In this method, aliquots of oxidant are added to a solution of degenerately doped NCs with a known NC concentration. Absorption spectra are recorded after each addition, and the absorption intensity is plotted as a function of equivalents of added oxidant per NC, allowing electron densities to be measured directly.[21,25]

1.5 **Nanocrystal Doping Strategies**

Significant progress has been made in stabilizing excess charge carriers in many colloidal NC systems. Factors such as self-purification and surface reactivity, which previously made it difficult to stably introduce excess charges into NC band-edges, have been overcome in many NC

systems, most notable in II-, III-, and IV-VI oxides and chalcogenide systems.[11,14,18-19,21,23-25] These advances have allowed researchers to carefully study various optoelectronic and redox properties of NCs. The most prevalent strategies for preparing degenerately doped NCs are discussed below.

1.5.1 *Chemical reduction/oxidation*

Molecules with strongly reducing formal potentials can inject charge carriers into NCs. This process was first demonstrated by the Guyot-Sionnest group when the authors used sodium biphenyl to inject charges into CdSe NCs.[14] Upon mixing the NCs with the reductant, they observed the characteristic absorption features of degenerate doping (Figure 1.2). The biphenyl radical has a more negative reduction potential than the CdSe CB-edge, providing a thermodynamic driving force for charge injection. The Klimov group achieved charge carrier injection using the more-mild cobaltocene to reduce PbS and PbSe QDs.[19] In both cases, an excess of reductant molecules relative to NCs is needed to achieve doping. Similarly, *p*-doped $Cu_{2-x}S$ NCs have been prepared by chemical oxidation with ferrocenium molecules.[28]

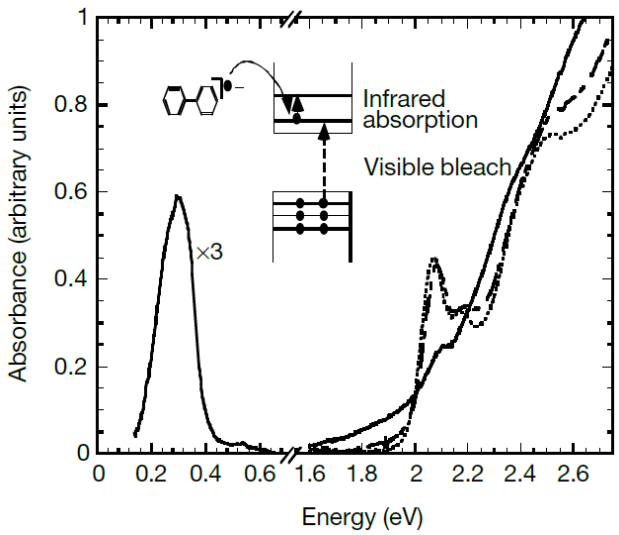

Figure 1.2. Absorption spectra of CdSe nanocrystals before (dotted line), immediately after (solid line), and 27 hours after (dashed line) the addition of sodium biphenyl. Reprinted with permission from ref.[14] Copyright 2000 Springer Nature

Molecular reductants often have deleterious effects on NCs. A blueshift is often observed in the absorption spectra of NCs that have been reoxidized after chemical reduction, indicative of surface etching.[14-15] Some studies suggest that chemical reductants induce irreversible reactions at CdSe NC surfaces and cause ligands to detach.[30] These side reactions rationalize the need for a stoichiometric excess of reductant for NC chemical doping. The presence of excess reductant also precludes quantitative titrations with oxidants to quantify NC electron densities.

1.5.2 *Electrochemical charge injection*

Application of a sufficiently reducing/oxidizing potential can inject charges into the quantum-confined states of NCs. Because it requires direct electrical contact with an electrical current, this process is limited to films deposited on conductive substrates. The Guyot-Sionnest group demonstrated electrochemical charge injection in films of CdSe[24] and PbSe QDs.[18] PbSe provides a rare example of NCs that can be tuned either *n*- or *p*-type by varying between negative

and positive applied potentials. Figure 1.3 shows differential absorption of PbSe QD films after a negative (top) or positive (bottom) potential is applied.[18] In both cases, an excitonic absorption bleach is observed at ~ 5000 cm^{-1} along with an induced absorption feature at ~ 1600 cm^{-1}, consistent with injection of CB electrons or VB holes.

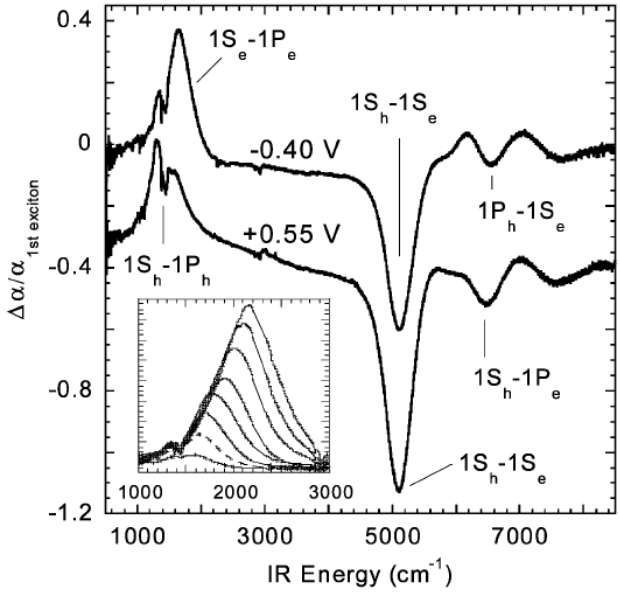

Figure 1.3. Difference spectra for a film of d = 7.2 nm diameter PbSe ADs at -0.40 and +0.55 V, offset for clarity. The inset shows the induced absorption for a series of voltages between -0.35 and -0.70 V; the dotted line is the feature at -0.40 V. Solvent absorption peaks in the 1000–2000 cm^{-1} range disrupt the induced absorption feature. Reprinted with permission from ref.[18] Copyright 2003 American Chemical Society

Doped metal-oxide NCs with LSPR absorption in the NIR are particularly attractive as components for smart window applications for buildings.[2,26,31] The LSPR absorption intensity can be increased or decreased by an applied potential. An increase in NIR absorption in smart windows leads to less transmittance of solar NIR photons into the building, resulting in less heating and better energy management.

While electrochemical doping provides rapid cycling between various redox states of NCs, it has some disadvantages. Nanocrystal films are often degraded under applied potential, limiting

their viability as robust components in applications. Various film treatments, such as ligand exchange and annealing, are required to stabilize these films.[18,26] These treatments change the electronic properties of the NC,[32] making it difficult to correlate properties of colloidal NCs with NC films. Additionally, the charges added to the NCs are not stable; they require a current to be applied continuously.

1.5.3 *Aliovalent doping*

Aliovalent doping is accomplished by creating a charge imbalance in the lattice of NCs. Most commonly, lattice cations are substituted by cations of a higher oxidation state. These aliovalent cations are thought to stabilize the CB below the Fermi level of the solution, facilitating the injection of charges into the NC by some external reservoir.[25,33] For example, in aluminum-doped ZnO (AZO), Zn^{2+} cations are substituted with Al^{3+} cations. A fraction of these excess positive charges (generally less than 15%) are compensated by CB electrons.[33-34] Another common material is tin-doped indium oxide (ITO). In this case, Sn^{4+} cations replace In^{3+} cations. AZO and ITO NCs have high electron doping densities and exhibit LSPR absorption.

The unusual capability for PbSe NCs to incorporate electrons or holes is further demonstrated by aliovalent doping. Both *n*-type[12] and *p*-type[35] PbSe NCs can be achieved through aliovalent doping with Ag^{+} and In^{3+} ions, respectively. In this case, aliovalent doping was achieved post-synthetically through partial cation exchange with Ag^{+} or In^{3+} salts.

Lattice stoichiometry can also lead to degenerately doped NCs. The deficiency or excess of metal ions can create a charge imbalance that facilitates the introduction of charges into the bands. Copper-deficient $Cu_{2-x}S$ and $Cu_{2-x}Se$ NCs, for example, exhibit LSPR absorption.[20,28] In this case, the material contains copper vacancies, which are charge-compensated by VB holes.

Gallium iron oxide ($FeGa_2O_4$) is a unique example where stoichiometry can be used to turn on *n*-type or *p*-type behavior.[36] Ga^{3+} -rich NCs are *n*-type, whereas Fe^{2+} -rich NCs are *p*-type. This doping was verified by absorption and photovoltage measurements.

1.5.4 *Photodoping*

Photodoping is a post-synthetic technique for preparing degenerately-doped colloidal NCs. In this process, an anaerobic solution of NCs is photoexcited in the presence of sacrificial reductant molecules.[21] The photogenerated VB hole is rapidly quenched by the sacrificial reductant, leaving excess electrons in the CB that are charge-compensated by cationic surface species (Scheme 1.2). Photodoping provides the advantages of being reversible and tunable. Since it generally does not damage NCs, excellent optical spectra are obtained, facilitating studies with advanced spectroscopic techniques. Finally, photodoped NCs are amenable to quantitative titrations because they are not in solution with excess redox-active molecules, as would be the case with chemical reduction.

Scheme 1.2. Photodoping Mechanism. Reprinted with permission from ref.[21] Copyright 2013 American Chemical Society

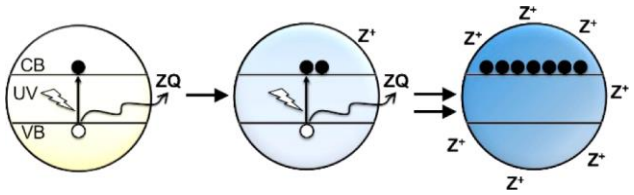

Photodoped ZnO NCs are the model platform for many research studies. The effect of different hole quenchers on maximum doping density,[21] the limiting mechanisms of maximum photodoping,[22] the redox properties of excess electrons,[22,37-38] the coupling between excess electrons and magnetic dopants,[39] and the luminescence dynamics in photodoped ZnO have been

thoroughly explored.[40] These studies highlight the versatility of photodoping as a means for preparing stable, degenerately doped NCs with high optical quality.

Interestingly, CdSe NCs are photodoped by a multistep process. Early studies showed that Li[Et_3BH] is an efficient hole-quencher for cadmium chalcogenide NCs.[15] Further investigation showed that photodoping can be achieved with a wide variety of reductants.[41] This work showed that photodoping in CdSe NCs occurs by first undergoing a dark reduction of surface species, such as pre-existing oxidized selenium species (*e.g.*, Se_2^-). These reduced species subsequently quench photogenerated holes, leaving delocalized electrons in the CB.

1.6 **Electrochemical Techniques for Studying Nanocrystal Redox Properties**

While spectroscopic measurements of degenerately doped NCs are relatively straightforward, direct measurement of their redox properties is more challenging. An understanding of NC redox properties is essential if they are to be used in any devices involving charge transfer, such as photovoltaics, photocatalysis, or light-emitting diodes. Hence, electrochemical techniques are necessary to measure the redox properties of degenerately doped NCs. Below, two techniques for directly measuring NC redox properties are highlighted.

1.6.1 *Cyclic Voltammetry*

Cyclic voltammetry (CV) is a common electrochemical characterization technique. CV affords such information as changes in redox states, coulombic efficiency, and electrochemical reversibility of compounds. In this technique, an applied voltage is cycled at a working electrode and the system's resulting current is measured. CV has been commonly applied to infer the band-edge potentials of NCs.[42-44] Figure 1.4 typifies CV data for colloidal CdSe NCs recorded at a glassy

carbon electrode in the presence (a) and absence (b) of CdSe QDs. As shown in Fig. 1.4, the cathodic (C1) and anodic (A1) peaks attributed to NC band-edge redox events are typically irreversible, adding complexity to interpretation of NC CVs. These signals are often overshadowed by background signals that can be attributed to surface redox events.

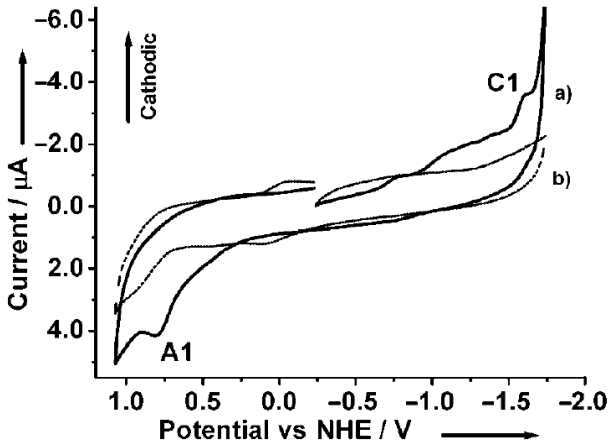

Figure 1.4. Cyclic voltammograms with (a) and without (b) CdSe QDs (1 mg mL^{-1}) dispersed in DMSO-toluene mixture. A1 and C1 denote the anodic and cathodic peaks, respectively. Reprinted with permission from ref.[43] Copyright 2008 Wiley

1.6.2 *Spectroelectrochemical Potentiometry*

Spectroelectrochemical potentiometry has emerged as a powerful tool for interrogating various redox properties of degenerately doped nanocrystals.[7-8,28,37,45] Potentiometry differs from electrochemical charge injection (voltammetric) methods in that no potential is applied to the NCs. Instead, the open circuit voltage (V_{OC}) of NC colloids is measured. The V_{OC} directly measures the E_F of the solution, which is in direct equilibrium with the E_F of the NCs.[37] Therefore, this method measures the E_F of colloidal NCs. More importantly, spectroelectrochemical potentiometry measures changes in the Fermi level of NCs while simultaneously measuring absorption spectra. This combination of quantitative spectroscopic measurements with potentiometry allows changes

in the NC E_F to be directly correlated with the addition or removal of charges from the NC bands, thereby providing direct measurement of NC redox properties.

Scheme 1.3. Schematic representation of spectroelectrochemical cell (Left). Fermi level change from undoped NCs (Middle) to photodoped NCs (Right). Reprinted with permission from ref.[37] Copyright 2016 American Chemical Society

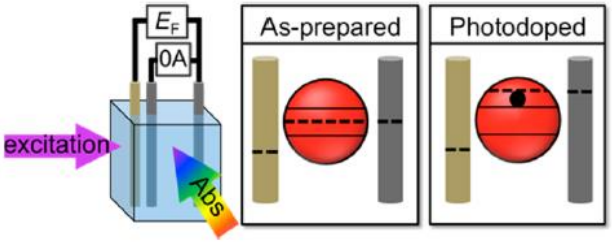

Scheme 1.3 illustrates the experimental setup for a typical spectroelectrochemical potentiometry measurement. A solution of NCs and supporting electrolyte is prepared in a cuvette containing a reference electrode, counter electrode, and working electrode (scheme 1.3, left). The potentiostat measures the V_{OC} of the solution (*i.e.*, the E_F of the NCs) under galvanostatic control (I = 0 A) at the working electrode with respect to the reference electrode (scheme 1.3, middle). When the NCs are photodoped, the E_F raises into the CB (scheme 1.3, right) and the working electrode equilibrates accordingly, as indicated by a change in the V_{OC} to a more negative potential. Meanwhile, absorption spectra are recorded throughout the potentiometric measurement.

Figure 1.5A shows typical results from a spectroelectrochemical potentiometry measurement on photodoped ZnO NCs. Potentiometric (blue) and absorption (λ = 1000 nm, black) data for d = 6.8 nm ZnO NCs were recorded as a function of photodoping time. The absorbance increases and the E_F becomes more negative with time, consistent with the addition of electrons into the CB. Because the absorption and potentiometric data are measured concurrently, these data can be plotted as E_F *vs* $\langle n \rangle$ (Figure 1.5B). Figure 1.5B highlights the strength of

spectroelectrochemical potentiometry for directly measuring redox properties of NCs. The red trace shows that E_F increases as electrons are added to the CB. Importantly, the CB-edge potential is given by E_F at $\langle n \rangle$ = 1. Knowledge of NC band-edge potentials is important for the rational design of devices, where efficiency is dependent on the thermodynamic driving force for charge migration. This technique is an elegant way of directly measuring this property in colloidal NCs, foregoing the need to rely on assumptions based on the band-edge potentials of bulk semiconductors.

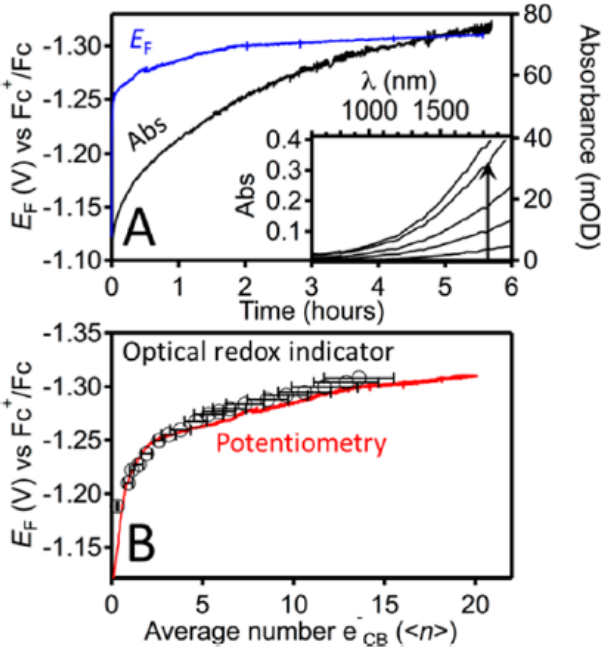

Figure 1.5. (A) Potentiometry (blue) and electronic absorption (black, λ = 1000 nm) data collected during photodoping of d = 6.8 nm ZnO NCs using EtOH as the hole quencher. A 14:1 THF/toluene solution of 0.1 μM tetrabutylammonium hexafluorophosphate ($TBAPF_6$), 660 μM $[Cp_2Co][PF_6]$ was irradiated at 340 nm while stirring. The inset shows NIR absorption spectra of the same ZnO NCs growing with increasing $\langle n \rangle$. (B) Plot of E_F *vs* $\langle n \rangle$ for photodoped ZnO NCs derived from potentiometric (red curve) and optical redox indicator (black circles) methods. $\langle n \rangle$ was determined spectroscopically. The error bars represent ± σ from the mean. E_F is referenced to the Fc^+/Fc redox couple. Reprinted with permission from ref.[37] Copyright 2016 American Chemical Society

1.7 **Charge Carrier Stabilization and Redox Properties**

Degenerately doped NCs must maintain overall charge neutrality, either by charge-compensation through counter ions at the surface or aliovalent dopants in the lattice. The motif of charge compensation plays a significant role in the electronic properties of the NC and the redox properties of the excess charge carriers themselves. Rational control of NC band-edge energies facilitates the design of multi-component photovoltaics where band offsets strongly influence device efficiency.

1.7.1 *Surface compensation*

Nanocrystal surfaces play a critical role in the physical and electronic properties of NCs. Researchers have investigated how ligands enable dissolution of NCs into colloids, enhance stability, and enable the formation of superlattices.[46-47] Ligand studies have also demonstrated the impact of ligand dipoles on the band-edge energies of NCs. It was shown that PbS band-edge potentials can be tuned by 1–2 eV depending on ligand choice.[32,48] This band-edge tunability is much larger than what is accessible through quantum confinement alone.

n-type photodoped and chemically doped NCs are charge-compensated by cationic species at the surface. The nature of these counter ions and their proximity to the NC surface greatly influences the redox properties of the CB electrons.[22,38] Potentiometric titration data of photodoped ZnO NCs show that the Fermi level becomes more negative (destabilized) when protons are removed from the surface and replaced with bulkier cations.[38] Similarly, electrons are ~ 600 mV more negative (destabilized) in ZnO NCs that are reduced by bulky decamethylcobaltocene (charge-compensated by decamethylcobaltocenium) relative to photodoped NCs that are charge-compensated by protons.[22] These observations show that bulkier cations that are further from the

surface are less effective at stabilizing CB electrons. Meanwhile, smaller cations, such as Li^+ or H^+, can get closer to the surface, bond to surface ions, or even intercalate into the NC, providing a much higher stabilization of the CB electrons.

The importance of surface counter ion proximity is further illustrated in a study by the Houtepen group on electrochemically doped NC films in high melting-point solvents.[49] The researchers electrochemically reduced films of NCs at high temperature before decreasing the temperature to freeze the solvent. By freezing the solvent, counter ions were effectively frozen at the NC surface, thereby enhancing the stability of the doped NCs compared to acetonitrile solvent, where the counter ions can move away from the surface and lead to NC discharge.

1.7.2 *Lattice compensation*

Lattice-compensated charges are generally more stable in ambient conditions than surface-compensated charges. A clear example is the comparison between AZO and photodoped ZnO. While these materials may be spectroscopically identical, their redox properties are vastly different. Decamethylferrocenium, a mild oxidant, can remove electrons from anaerobic solutions of photodoped ZnO, but the same oxidant does not remove any of the Al^{3+}-compensated electrons from AZO.[33] Similar behavior is observed between In_2O_3 and ITO.[25] In aliovalently doped materials, it is hypothesized that aliovalent dopants stabilize the CB relative to the undoped material rather than raising the Fermi level (Scheme 1.4). This is an important distinction that determines the redox reactivity of excess electrons.

Scheme 1.4. Conduction band stabilization in aliovalently-doped nanocrystals. Reprinted from ref.[25] Copyright 2014 American Chemical Society

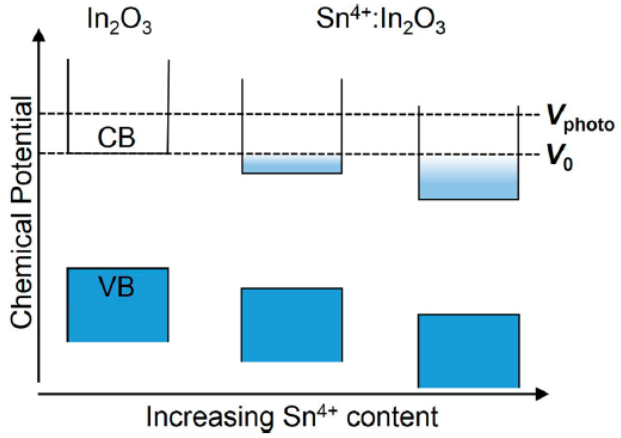

Direct measurement of the energetic stabilization of aliovalent *vs* surface charge compensation was first demonstrated in $Cu_{2-x}S$ NCs (Figure 1.6).[28] *p*-type $Cu_{2-x}S$ NCs with equal hole densities (Fig. 1.6A) were prepared either by outer sphere oxidation with ferrocenium triflate (surface charge compensation) or by removal of Cu^+ ions (lattice charge compensation). These copper vacancies provide the same electrostatic effect as aliovalent dopants. Potentiometric measurements showed that holes in the copper-deficient NCs were stabilized by ~ 300 mV relative to the NCs oxidized by ferrocenium (Fig. 1.6B). The difference in redox properties between surface and lattice charge-compensation motifs is studied in further detail in chapter 3.

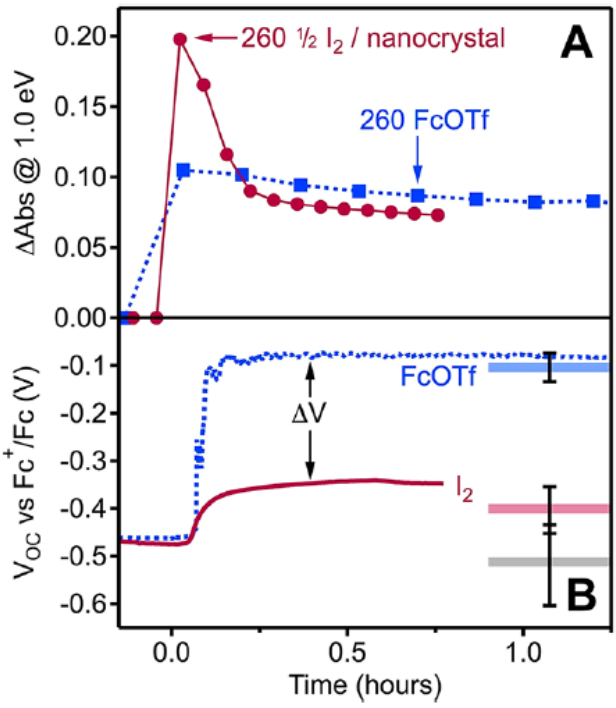

Figure 1.6. (A) Differential absorption at 1.0 eV for d = 5.4 nm $Cu_{2-x}S$ NCs oxidized with 260 equiv. of 1/2 I_2 (solid red) or FcOTf (dashed blued). (B) V_{OC} plotted *vs* time for the data in panel B. Shaded boxes and vertical error bars indicate the mean and standard deviation in V_{eq} from multiple measurements on nanocrystals prior to oxidation (20 measurements), and after addition of 260 equiv. of either Fc^+ (2 measurements with FcOTf, 3 with $FcBF_4$) or 1/2 I_2 (3 measurements). Reprinted with permission from ref.[28] Copyright 2018 American Chemical Society

1.8 Summary

In summary, nanocrystals continue to be a highly productive area of research. They offer many opportunities for interesting new fundamental science and for the development of exciting new technologies. The ability to controllably dope NCs broadens the scope of these materials and enables many new areas of research that are not possible in undoped NCs. Various methods, such as photodoping, have been developed and matured for preparing degenerately doped NCs. These methods allow photophysical and redox properties of NCs to be interrogated. Degenerately doped NCs exhibit quantitative changes in their electronic absorption spectra, including excitonic

absorption bleach and new lower-energy absorption from the excess charge carriers. Spectroelectrochemical techniques give information about the CB-edge potentials, surface redox chemistry, and charge stabilization in doped NCs. The redox potentials of excess charge carriers are determined by factors such as charge-compensation motif and surface chemistry, even for excess charge carriers that are spectroscopically identical.

1.9 **References**

1. Talapin, D. V.; Lee, J. S.; Kovalenko, M. V.; Shevchenko, E. V., Prospects of colloidal nanocrystals for electronic and optoelectronic applications. *Chem. Rev.* **2010,** *110*, 389-458.
2. Runnerstrom, E. L.; Llordes, A.; Lounis, S. D.; Milliron, D. J., Nanostructured electrochromic smart windows: traditional materials and NIR-selective plasmonic nanocrystals. *Chem. Commun.* **2014,** *50*, 10555-72.
3. Comin, A.; Manna, L., New materials for tunable plasmonic colloidal nanocrystals. *Chem. Soc. Rev.* **2014,** *43*, 3957-75.
4. Hillhouse, H. W.; Beard, M. C., Solar cells from colloidal nanocrystals: Fundamentals, materials, devices, and economics. *Curr. Opin. Colloid In.* **2009,** *14*, 245-259.
5. Smith, A. M.; Nie, S., Semiconductor nanocrystals: structure, properties, and band gap engineering. *Acc. Chem. Res.* **2010,** *43*, 190-200.
6. Schimpf, A. M.; Knowles, K. E.; Carroll, G. M.; Gamelin, D. R., Electronic doping and redox-potential tuning in colloidal semiconductor nanocrystals. *Acc. Chem. Res.* **2015,** *48*, 1929-37.
7. Carroll, G. M.; Tsui, E. Y.; Brozek, C. K.; Gamelin, D. R., Spectroelectrochemical Measurement of Surface Electrostatic Contributions to Colloidal CdSe Nanocrystal Redox Potentials. *Chem. Mater.* **2016,** *28*, 7912-7918.
8. Brozek, C. K.; Zhou, D.; Liu, H.; Li, X.; Kittilstved, K. R.; Gamelin, D. R., Soluble Supercapacitors: Large and Reversible Charge Storage in Colloidal Iron-Doped ZnO Nanocrystals. *Nano Lett.* **2018,** *18*, 3297-3302.
9. Hartstein, K. H.; Erickson, C. S.; Tsui, E. Y.; Marchioro, A.; Gamelin, D. R., Electron Stability and Negative-Tetron Luminescence in Free-Standing Colloidal n-Type CdSe/CdS Quantum Dots. *ACS Nano* **2017,** *11*, 10430-10438.
10. Hughes, K. E.; Hartstein, K. H.; Gamelin, D. R., Photodoping and Transient Spectroscopies of Copper-Doped CdSe/CdS Nanocrystals. *ACS Nano* **2018,** *12*, 718-728.
11. Araujo, J. J.; Brozek, C. K.; Kroupa, D. M.; Gamelin, D. R., Degenerately n-Doped Colloidal PbSe Quantum Dots: Band Assignments and Electrostatic Effects. *Nano Lett.* **2018,** *18*, 3893-3900.
12. Lu, H.; Carroll, G. M.; Chen, X.; Amarasinghe, D. K.; Neale, N. R.; Miller, E. M.; Sercel, P. C.; Rabuffetti, F. A.; Efros, A. L.; Beard, M. C., n-Type PbSe Quantum Dots via Post-Synthetic Indium Doping. *J. Am. Chem. Soc.* **2018,** *140*, 13753-13763.
13. An, J. M.; Franceschetti, A.; Zunger, A., Pauli blocking versus electrostatic attenuation of optical transition intensities in chargedPbSequantum dots. *Phys. Rev. B* **2007,** *76*.
14. Shim, M.; Guyot-Sionnest, P., n-type colloidal semiconductor nanocrystals. *Nature* **2000,** *407*, 981-3.
15. Rinehart, J. D.; Schimpf, A. M.; Weaver, A. L.; Cohn, A. W.; Gamelin, D. R., Photochemical electronic doping of colloidal CdSe nanocrystals. *J. Am. Chem. Soc.* **2013,** *135*, 18782-5.
16. Jeong, K. S.; Deng, Z.; Keuleyan, S.; Liu, H.; Guyot-Sionnest, P., Air-Stable n-Doped Colloidal HgS Quantum Dots. *J. Phys. Chem. Lett.* **2014,** *5*, 1139-43.
17. Deng, Z.; Jeong, K. S.; Guyot-Sionnest, P., Colloidal quantum dots intraband photodetectors. *ACS Nano* **2014,** *8*, 11707-14.
18. Wehrenberg, B. L.; Guyot-Sionnest, P., Electron and hole injection in PbSe quantum dot films. *J. Am. Chem. Soc.* **2003,** *125*, 7806-7.

19. Koh, W. K.; Koposov, A. Y.; Stewart, J. T.; Pal, B. N.; Robel, I.; Pietryga, J. M.; Klimov, V. I., Heavily doped n-type PbSe and PbS nanocrystals using ground-state charge transfer from cobaltocene. *Sci. Rep.* **2013,** *3*, 2004.
20. Luther, J. M.; Jain, P. K.; Ewers, T.; Alivisatos, A. P., Localized surface plasmon resonances arising from free carriers in doped quantum dots. *Nat. Mater.* **2011,** *10*, 361-6.
21. Schimpf, A. M.; Gunthardt, C. E.; Rinehart, J. D.; Mayer, J. M.; Gamelin, D. R., Controlling carrier densities in photochemically reduced colloidal ZnO nanocrystals: size dependence and role of the hole quencher. *J. Am. Chem. Soc.* **2013,** *135*, 16569-77.
22. Carroll, G. M.; Schimpf, A. M.; Tsui, E. Y.; Gamelin, D. R., Redox Potentials of Colloidal n-Type ZnO Nanocrystals: Effects of Confinement, Electron Density, and Fermi-Level Pinning by Aldehyde Hydrogenation. *J. Am. Chem. Soc.* **2015,** *137*, 11163-9.
23. Shim, M.; Wang, C.; Guyot-Sionnest, P., Charge-Tunable Optical Properties in Colloidal Semiconductor Nanocrystals. *J. Phys. Chem. B* **2001,** *105*, 2369-2373.
24. Wang, C.; Shim, M.; Guyot-Sionnest, P., Electrochromic nanocrystal quantum dots. *Science* **2001,** *291*, 2390-2.
25. Schimpf, A. M.; Lounis, S. D.; Runnerstrom, E. L.; Milliron, D. J.; Gamelin, D. R., Redox chemistries and plasmon energies of photodoped In_2O_3 and Sn-doped In_2O_3 (ITO) nanocrystals. *J. Am. Chem. Soc.* **2015,** *137*, 518-24.
26. Zandi, O.; Agrawal, A.; Shearer, A. B.; Reimnitz, L. C.; Dahlman, C. J.; Staller, C. M.; Milliron, D. J., Impacts of surface depletion on the plasmonic properties of doped semiconductor nanocrystals. *Nat. Mater.* **2018,** *17*, 710-717.
27. Crockett, B. M.; Jansons, A. W.; Koskela, K. M.; Johnson, D. W.; Hutchison, J. E., Radial Dopant Placement for Tuning Plasmonic Properties in Metal Oxide Nanocrystals. *ACS Nano* **2017,** *11*, 7719-7728.
28. Hartstein, K. H.; Brozek, C. K.; Hinterding, S. O. M.; Gamelin, D. R., Copper-Coupled Electron Transfer in Colloidal Plasmonic Copper-Sulfide Nanocrystals Probed by in Situ Spectroelectrochemistry. *J. Am. Chem. Soc.* **2018,** *140*, 3434-3442.
29. Hartstein, K. H.; Schimpf, A. M.; Salvador, M.; Gamelin, D. R., Cyclotron Splittings in the Plasmon Resonances of Electronically Doped Semiconductor Nanocrystals Probed by Magnetic Circular Dichroism Spectroscopy. *J. Phys. Chem. Lett.* **2017,** *8*, 1831-1836.
30. Hartley, C. L.; Dempsey, J. L., Electron-Promoted X-Type Ligand Displacement at CdSe Quantum Dot Surfaces. *Nano Lett.* **2019,** *19*, 1151-1157.
31. Kriegel, I.; Scotognella, F.; Manna, L., Plasmonic doped semiconductor nanocrystals: Properties, fabrication, applications and perspectives. *Phys. Rep.* **2017,** *674*, 1-52.
32. Brown, P. R.; Kim, D.; Lunt, R. R.; Zhao, N.; Bawendi, M. G.; Grossman, J. C.; Bulovic, V., Energy level modification in lead sulfide quantum dot thin films through ligand exchange. *ACS Nano* **2014,** *8*, 5863-72.
33. Schimpf, A. M.; Ochsenbein, S. T.; Buonsanti, R.; Milliron, D. J.; Gamelin, D. R., Comparison of extra electrons in colloidal n-type Al(3+)-doped and photochemically reduced ZnO nanocrystals. *Chem. Commun.* **2012,** *48*, 9352-4.
34. Zhou, D.; Wang, P.; Roy, C. R.; Barnes, M. D.; Kittilstved, K. R., Direct Evidence of Surface Charges in n-Type Al-Doped ZnO. *J. Phys. Chem. C* **2018,** *122*, 18596-18602.
35. Kroupa, D. M.; Hughes, B. K.; Miller, E. M.; Moore, D. T.; Anderson, N. C.; Chernomordik, B. D.; Nozik, A. J.; Beard, M. C., Synthesis and Spectroscopy of Silver-Doped PbSe Quantum Dots. *J. Am. Chem. Soc.* **2017,** *139*, 10382-10394.

36. Urso, C.; Barawi, M.; Gaspari, R.; Sirigu, G.; Kriegel, I.; Zavelani-Rossi, M.; Scotognella, F.; Manca, M.; Prato, M.; De Trizio, L.; Manna, L., Colloidal Synthesis of Bipolar Off-Stoichiometric Gallium Iron Oxide Spinel-Type Nanocrystals with Near-IR Plasmon Resonance. *J. Am. Chem. Soc.* **2017,** *139*, 1198-1206.
37. Carroll, G. M.; Brozek, C. K.; Hartstein, K. H.; Tsui, E. Y.; Gamelin, D. R., Potentiometric Measurements of Semiconductor Nanocrystal Redox Potentials. *J. Am. Chem. Soc.* **2016,** *138*, 4310-3.
38. Brozek, C. K.; Hartstein, K. H.; Gamelin, D. R., Potentiometric Titrations for Measuring the Capacitance of Colloidal Photodoped ZnO Nanocrystals. *J. Am. Chem. Soc.* **2016,** *138*, 10605-10.
39. Beaulac, R.; Schneider, L.; Archer, P. I.; Bacher, G.; Gamelin, D. R., Light-induced spontaneous magnetization in doped colloidal quantum dots. *Science* **2009,** *325*, 973-6.
40. Cohn, A. W.; Janßen, N.; Mayer, J. M.; Gamelin, D. R., Photocharging ZnO Nanocrystals: Picosecond Hole Capture, Electron Accumulation, and Auger Recombination. *J. Phys. Chem. C* **2012,** *116*, 20633-20642.
41. Tsui, E. Y.; Hartstein, K. H.; Gamelin, D. R., Selenium Redox Reactivity on Colloidal CdSe Quantum Dot Surfaces. *J. Am. Chem. Soc.* **2016,** *138*, 11105-8.
42. Haram, S. K.; Quinn, B. M.; Bard, A. J., Electrochemistry of CdS nanoparticles: a correlation between optical and electrochemical band gaps. *J. Am. Chem. Soc.* **2001,** *123*, 8860-1.
43. Inamdar, S. N.; Ingole, P. P.; Haram, S. K., Determination of band structure parameters and the quasi-particle gap of CdSe quantum dots by cyclic voltammetry. *ChemPhysChem* **2008,** *9*, 2574-9.
44. Amelia, M.; Lincheneau, C.; Silvi, S.; Credi, A., Electrochemical properties of CdSe and CdTe quantum dots. *Chem. Soc. Rev.* **2012,** *41*, 5728-43.
45. Tsui, E. Y.; Carroll, G. M.; Miller, B.; Marchioro, A.; Gamelin, D. R., Extremely Slow Spontaneous Electron Trapping in Photodoped n-Type CdSe Nanocrystals. *Chem. Mater.* **2017,** *29*, 3754-3762.
46. Choi, J. J.; Bealing, C. R.; Bian, K.; Hughes, K. J.; Zhang, W.; Smilgies, D. M.; Hennig, R. G.; Engstrom, J. R.; Hanrath, T., Controlling nanocrystal superlattice symmetry and shape-anisotropic interactions through variable ligand surface coverage. *J. Am. Chem. Soc.* **2011,** *133*, 3131-8.
47. Weidman, M. C.; Nguyen, Q.; Smilgies, D.-M.; Tisdale, W. A., Impact of Size Dispersity, Ligand Coverage, and Ligand Length on the Structure of PbS Nanocrystal Superlattices. *Chem. Mater.* **2018,** *30*, 807-816.
48. Kroupa, D. M.; Voros, M.; Brawand, N. P.; McNichols, B. W.; Miller, E. M.; Gu, J.; Nozik, A. J.; Sellinger, A.; Galli, G.; Beard, M. C., Tuning colloidal quantum dot band edge positions through solution-phase surface chemistry modification. *Nat. Commun.* **2017,** *8*, 15257.
49. Gudjonsdottir, S.; van der Stam, W.; Koopman, C.; Kwakkenbos, B.; Evers, W. H.; Houtepen, A. J., On the Stability of Permanent Electrochemical Doping of Quantum Dot, Fullerene, and Conductive Polymer Films in Frozen Electrolytes for Use in Semiconductor Devices. *ACS Appl. Nano Mater.* **2019,** *2*, 4900-4909.

Chapter 2. Degenerately *n*-Doped Colloidal PbSe Quantum Dots: Band Assignments and Electrostatic Effects

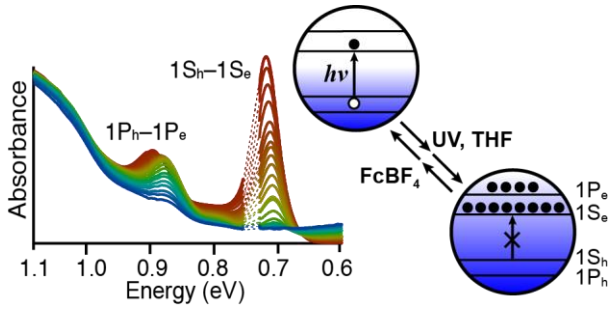

Reproduced with permission from Araujo, J.; Brozek, C.; Kroupa, M. and Gamelin, R. *Nano Lett.* **2018**, 18, 3893−3900. Copyright 2018 American Chemical Society

2.1 **Overview**

We present a spectroscopic study of colloidal PbSe quantum dots (QDs) that have been photodoped to introduce excess delocalized conduction-band (CB) electrons. High-quality absorption spectra are obtained for these degenerately doped QDs with excess-electron concentrations up to ~10^{20} cm^{-3}. At the highest doping levels, electrons have completely filled the $1S_e$ orbitals of the CB and partially populate the higher-energy $1P_e$ orbitals. Spectroscopic changes observed as a function of carrier concentration permit unambiguous assignment of the second excitonic absorption maximum to $1P_h$-$1P_e$ transitions. At intermediate doping levels, a clear absorption feature appears between the first two excitonic maxima that is attributable to parity-forbidden $1S_{h,e}$-$1P_{e,h}$ excitations, observable because of electrostatic symmetry breaking. Redshifts of the main excitonic absorption features with increased carrier concentration are also analyzed. The Coulomb stabilization energies of both the $1S_h$-$1S_e$ and $1P_h$-$1P_e$ excitons in *n*-doped PbSe QDs are remarkably similar to those observed for multiexcitons with the same electron count. The origins of these redshifts are discussed.

2.2 **Introduction**

PbSe quantum dots (QDs) are important narrow-gap semiconductor materials for photovoltaic[1-5] and photodetector applications.[6] Their rocksalt structure, large Bohr radius, nearly symmetric band structure, and eightfold band-edge degeneracy make PbSe QDs particularly interesting for fundamental QD electronic-structure and photophysical studies, including of quantum-confinement effects, multiple exciton generation (MEG),[7-8] and hot-carrier dynamics.[9] Despite broad and longstanding interest in the spectroscopic properties of PbSe QDs, the correct assignment of their characteristic electronic absorption features, and particularly the second absorption maximum, has been the subject of several conflicting studies spanning more than a decade and persisting in recent literature.

Early theoretical work[10-11] and subsequent two-photon photoluminescence excitation data[12] proposed assignment of the second maximum as a combination of parity-forbidden $1S_h$-$1P_e$ and $1P_h$-$1S_e$ transitions (abbreviated here as $1S_{h,e}$-$1P_{e,h}$) that gain allowedness *via* symmetry-breaking perturbations. Other experimental work based on scanning tunneling microscopy (STM)[13] and transient-absorption (TA)[14] measurements concluded that the correct assignment of this feature is instead as $1P_h$-$1P_e$ excitations. In this assignment, the $1S_{h,e}$-$1P_{e,h}$ transitions were anticipated to reside between the first two absorption maxima, where only broad and featureless baseline absorption is typically observed. Induced absorption between the $1S_h$-$1S_e$ and $1P_h$-$1P_e$ peaks has been observed in transient-absorption (TA) measurements and attributed to these forbidden $1S_{h,e}$-$1P_{e,h}$ transitions.[15-16] The substantial background signal between these two maxima in normal absorption spectra is not easily explained, however. For example, Rayleigh scattering[17] and local-field effects[18] have been proposed. Without a clear understanding of its origins, disambiguation of

TA signals in this region is challenging because of the possibility that this relatively intense background may itself change upon photoexcitation.

More recently,[19] spectral changes with QD electronic doping were analyzed and concluded to indicate assignment of the second maximum as the $1S_{h,e}$-$1P_{e,h}$ band, not the $1P_h$-$1P_e$ band concluded from TA and STM studies. Electronic doping is a powerful way to perturb the electronic structures and physical properties of QDs. Excess delocalized carriers have been introduced into PbSe QDs electrochemically,[20] using aliovalent dopants,[21] using molecular reductants,[19] and in electrolyte-gated transistors employing 2D PbSe QD superlattices.[22] In contrast with the many TA studies of PbSe QDs with multiple excitons, however, there has been relatively little work on PbSe QDs with excess band-like electrons or holes. Given the long-standing discrepancy among spectral assignments, and given the relatively limited investigation of charged PbSe QDs to date, further spectroscopic examination of electronically doped PbSe QDs is warranted.

Here, we report photochemical electron injection into free-standing colloidal PbSe QDs of various diameters as a method for achieving tunable carrier concentrations reaching as high as ~10^{20} cm^{-3}, quantified optically and by oxidative titration. High-quality absorption spectra are obtained under these conditions, allowing investigation of the effects of static carrier accumulation using conventional continuous-wave methods. These absorption data show that the bleach of the often-debated second absorption maximum occurs *only after the bleach of the first absorption maximum*, contradicting the previous conclusion from *n*-doping and strongly supporting assignment of the second maximum as the $1P_h$-$1P_e$ band. Moreover, these data reveal electronic symmetry breaking and the appearance of a distinct $1S_{h,e}$-$1P_{e,h}$ absorption band between the first two maxima at elevated charging levels, precisely as predicted by theory.[23] This result represents the first static observation of a discrete $1S_{h,e}$-$1P_{e,h}$ absorption band in PbSe QDs. Finally, analysis

of PbSe QD absorption spectra collected as a function of excess electron density demonstrates exciton redshifts with *n*-doping that are surprisingly similar to those found for PbSe QD multiexcitons, despite the fact that compensating positive charges here are localized at the QD surfaces instead of delocalized within the QDs. The surprising insensitivity of the exciton redshifts to the position and localization of the positive charges is discussed. Electron correlation is proposed to dominate the exciton stabilization in these multi-carrier configurations.

2.3 **Results and Discussion**

Photodoping is an attractive strategy for introducing excess delocalized charge carriers into free-standing colloidal QDs of semiconductors such as ZnO[24-28] and CdE[29-31] (E = S, Se, Te). Spectroscopic and spectroelectrochemical investigations of photodoped QDs have yielded insights into trion-Auger dynamics,[32] trap-assisted-Auger processes,[33] QD surface redox reactivities,[30] and QD band-edge potentials.[34-36] Our initial attempts to photodope colloidal PbSe QDs followed the procedure of irradiating across the QD band gap in the presence of the reductant Li[Et_3BH], as detailed previously,[29] but these experiments caused considerable QD degradation (see Supporting Information, Fig. 2.4), possibly because of the effects of QD surface reduction,[30] and they failed to yield reliable photodoping results. In the course of experimentation, we discovered that irradiating neat THF solutions of colloidal PbSe QDs with an unfiltered Hg/Xe lamp induces significant bleaching of the first excitonic absorption band. This bleach recovers immediately upon exposing the QDs to air. Photolysis in toluene with dilute THF also yields the same spectral changes, but no photodoping occurs in the absence of THF, indicating that THF itself is directly involved. UV irradiation of THF is known to generate reactive radicals,[37-38] so we therefore hypothesized that similar UV photochemistry is responsible for the reactivity observed with PbSe

QDs (see Supporting Information). As a test of this hypothesis, we performed a control experiment in which the highest-energy photons ($\lambda \leq 280$ nm) from our Hg/Xe lamp, where THF absorbs, were filtered before the PbSe QD/THF solutions. We observed little to no photodoping in this experiment (see Supporting Information, Fig. 2.4), supporting the hypothesis that radicals from THF photolysis are responsible for QD reduction. Similarly, we observed slow deposition of polymerized organics onto the cuvette window with prolonged irradiation, again consistent with organic photolysis to generate radicals. In this regard, this photodoping is qualitatively different from that involving Li[Et_3BH], and it instead appears more closely analogous to radical reduction of ZnO nanocrystals initiated by pulse radiolysis.[24] Although detailed mechanistic studies of the THF photolysis and electron-transfer processes are considered beyond the scope of this study, the observation that photogenerated radicals can be used for chalcogenide QD reduction is noteworthy, introducing a facile and tunable method for preparing stable heavily *n*-doped QDs with excellent optical properties. Unlike chemical reduction of PbSe QDs using cobaltocene,[19] which requires ~10^3-fold excess reductant to achieve similar doping levels, the absence of excess reductant (radicals) in equilibrium with the reduced QDs formed by this photodoping method allows titration of the added electrons and opens the door to studies of these *n*-doped QDs without the complication of a solvated reductant reservoir.

Figure 2.1a shows absorption spectra of colloidal d = 6.2 nm PbSe QDs collected as a function of photodoping time. Amplitudes are plotted as absorbance and differential absorbance. Prior to photodoping, the absorption spectrum is dominated by the intense $1S_h$-$1S_e$ band centered at ~0.7 eV. The second maximum, observed at ~0.9 eV, is the feature that has been variously assigned to ($1S_h$-$1P_e$ + $1P_h$-$1S_e$)[10,12,19-20] or $1P_h$-$1P_e$ transitions.[13-14,39] As detailed below, the data here firmly support the latter assignment, and consequently this maximum is labeled $1P_h$-$1P_e$ in

Figure 2.1. With increasing photolysis time, the $1S_h$-$1S_e$ band bleaches and new intraband absorption appears in the infrared (see Supporting Information, Fig. 2.5), consistent with addition of electrons to the $1S_e$ CB orbitals. The $1P_h$-$1P_e$ band initially redshifts without any detectable intensity loss, as indicated by the derivative-shaped response at ~0.9 eV in the differential-absorption spectra for the first few photolysis intervals. After extensive photolysis, the $1S_h$-$1S_e$ absorption is fully bleached and the $1P_h$-$1P_e$ absorption also begins to bleach, as indicated by evolution of the derivative-shaped ΔA feature into a negative ΔA feature in this region. Photodoping also induces very broad and weak absorption that extends well below the first exciton. This absorption may stem from photoexcitation of reduced surface traps, but its proximity to other broad absorption (*e.g.*, between the two excitonic maxima) that remains incompletely understood makes this assignment tentative.

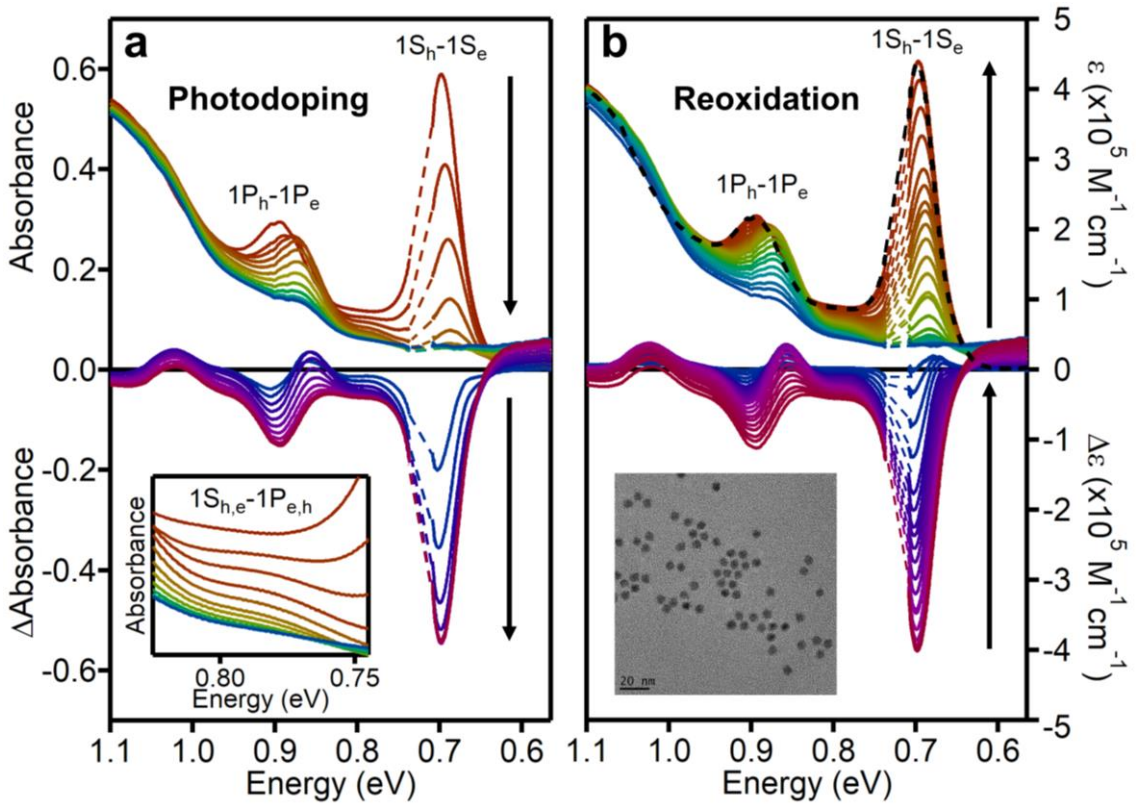

Figure 2.1. (a) Top: Absorption spectra of a THF solution of d = 6.2 nm PbSe QDs collected at various stages of photodoping. Bottom: Difference spectra ($\Delta A = A - A_0$). The inset shows a close-up of the absorption in the region between the $1S_h$-$1S_e$ and $1P_h$-$1P_e$ excitonic peaks (assigned to a combination of $1S_h$-$1P_e$ and $1P_h$-$1S_e$ transitions) during photodoping, see text. The arrows indicate the direction of increasing photodoping. (b) Top: Absorption spectra of the photodoped d = 6.2 nm PbSe QDs from panel a, collected at various stages of oxidative titration with $FcBF_4$. Bottom: Difference spectra ($\Delta A = A - A_0$). The black dashed line shows the absorption spectrum of the QDs prior to photodoping. The arrows indicate the direction of increasing oxidizing equivalents. The inset shows a TEM image of the d = 6.2 nm QDs used in the absorption measurements (scale bar = 20 nm). In both panels, the energy regions with intense solvent C-H stretching vibrations (0.707-0.737 eV) have been interpolated with dotted lines for clarity.

Figure 2.1b presents absorption spectra (plotted as ε, $M^{-1}cm^{-1}$) collected during reoxidation of the maximally photodoped PbSe QDs from Figure 2.1a by titration with $FcBF_4$. The entire absorption spectrum recovers as $FcBF_4$ equivalents are added to the QD solution, consistent with removal of the CB electrons added during photodoping. Oxidation also eliminates the weak sub-bandgap absorption, consistent with removal of trapped electrons. After enough $FcBF_4$ has been

added, the spectra no longer change with further $FcBF_4$ additions. The black dashed line represents the absorption spectrum of the same sample collected prior to photodoping, and shows that the spectrum recovers completely after cycling to maximum photodoping and then reoxidizing again, indicating that photodoping and reoxidation do not damage the QDs noticeably (see Supporting Information, Fig. 2.6 for TEM images before and after photodoping and titration).

Figure 2.2 summarizes the data from Figure 2.1, plotting the normalized bleaches of the $1S_h$-$1S_e$ and $1P_h$-$1P_e$ bands during photodoping and reoxidation as a function of photolysis time or added equivalents of $FcBF_4$ (see Supporting Information, Fig. 2.7 for fitting details). Figure 2.2a shows that the $1S_h$-$1S_e$ band begins to bleach immediately with photodoping, but the $1P_h$-$1P_e$ band does not begin to bleach until the $1S_h$-$1S_e$ band is ~85% bleached, and continues to bleach after the $1S_h$-$1S_e$ band is fully bleached. Figure 2.2b plots analogous data collected during oxidative titration with $FcBF_4$ (Figure 2.1b). Similar results are obtained for different-sized PbSe QDs (see Supporting Information, Fig. 2.8). The $1P_h$-$1P_e$ absorption begins to recover immediately when the first equivalents of $FcBF_4$ are added, but the $1S_h$-$1S_e$ absorption begins to recover only after multiple oxidizing equivalents have been added. The oxidation data in Figure 2.2b thus mirror the reduction data in Figure 2.2a, except that for one the x-axis is oxidizing equivalents and for the other it is photolysis time. To place both data sets on the same axes, we replot them as $-\Delta A/A_0$($1P_h$-$1P_e$) *vs* $-\Delta A/A_0$($1S_h$-$1S_e$) (Figure 2.2b, inset). Plotted this way, these data show that the spectral changes are identical in the reductive and oxidative directions of Figure 2.1. As stated above, these data firmly support assignment of the second absorption maximum as the $1P_h$-$1P_e$ band. If the second maximum were instead due to $1S_{h,e}$-$1P_{e,h}$ transitions, then it would also bleach with $1S_e$ orbital filling[14,16] (at half the rate of the $1S_h$-$1S_e$ bleach[19]), but such behavior is clearly not observed. The inset to Figure 2.2b highlights the fact that $1P_h$-$1P_e$ absorption does not begin to

bleach until *after* the $1S_h$-$1S_e$ absorption is almost completely bleached, and hence that it does not involve generation of $1S_e$ electrons.

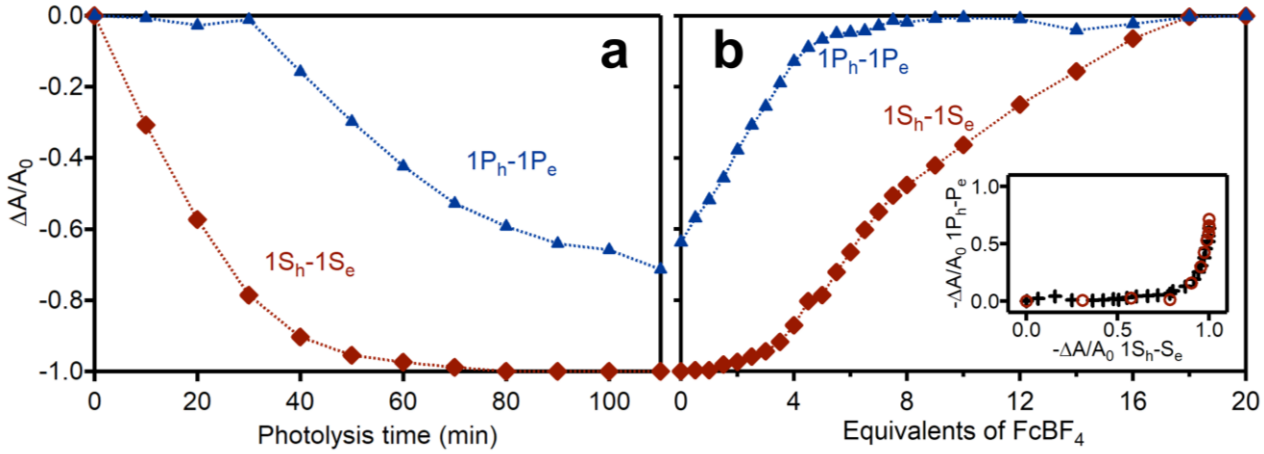

Figure 2.2. (a) Normalized differential absorbance of the $1S_h$-$1S_e$ (red diamonds) and $1P_h$-$1P_e$ (blue triangles) excitonic transitions of d = 6.2 nm PbSe QDs plotted as a function of photolysis time during photodoping. (b) Normalized differential absorbance of the $1S_h$-$1S_e$ (red diamonds) and $1P_h$-$1P_e$ (blue triangles) excitonic transitions plotted as a function of $FcBF_4$ equivalents added to the fully photodoped QDs from panel a. The inset plots $-\Delta A/A_0(1P_h\text{-}1P_e)$ *vs* $-\Delta A/A_0(1S_h\text{-}1S_e)$ from the data in panels a (red circles) and b (black crosses).

The average number of $1S_e$ CB electrons per QD can be determined optically from the bleach of the $1S_h$-$1S_e$ excitonic maximum according to $\langle n_{1Se}\rangle = 8 \times |\Delta A/A_0|$. The data in Figure 2.2 show that this absorption is completely bleached at maximum photodoping, and hence that the QDs contain at least 8 delocalized CB electrons. Optical determination of $\langle n_{tot}\rangle > 8$ can be approached in the same way. From the $1P_e$ degeneracy of 24, the value of $-\Delta A/A_0(1P_h\text{-}1P_e) \approx 0.65$ at maximum photodoping (Figure 2.2) implies accumulation of ~15 $1P_e$ electrons in these QDs, or $\langle n_{tot}\rangle \sim 23$ delocalized electrons, assuming a linear $1P_h$-$1P_e$ bleach with $1P_e$ filling. The titration data in Figure 2.2b provide an independent measure of the number of excess electrons in these QDs. Figure 2.2b shows that ~18 equivalents of oxidant are required to fully recover the initial

absorption spectrum following photodoping. Because the $1S_e$ level is eightfold degenerate, this result implies ~10 electrons distributed between the $1P_e$ orbitals and surface traps, in reasonable agreement with the optical estimate (15) if most or all of these 10 electrons occupy the $1P_e$ orbitals. Figure 2.2b shows, however, that the $1P_h$-$1P_e$ absorption bleach recovers rapidly with the first ~5 equivalents of $FcBF_4$, and subsequent additions initiate recovery of $1S_h$-$1S_e$ absorption. There is perhaps an additional slow recovery of remaining $1P_h$-$1P_e$ absorption with later additions. These titration data suggest accumulation of ~13 electrons per QD (~5 $1P_e$ + 8 $1S_e$ electrons) at maximum photodoping. There is thus a quantitative discrepancy between the optical and chemical values of the number of $1P_e$ electrons per QD determined from precisely the same data set. Nonetheless, all three metrics confirm that many delocalized electrons ($\langle n_{tot} \rangle \approx 13$–$23$, $\langle N \rangle \approx 10^{20}$ cm^{-3}) accumulate in the $1S_e$ and $1P_e$ levels under these photodoping conditions. We note that fewer electrons accumulate in smaller QDs than in larger QDs at maximum photodoping (see Supporting Information, Fig. 2.9), as observed for photodoped ZnO[28] and CdSe QDs[29] and chemically reduced PbSe QDs,[19] attributable in large part to the strong dependence of the Fermi level potential on carrier density (as opposed to the number of carriers).[28,35,40]

Interestingly, these high carrier densities are similar to those found in many plasmonic colloidal semiconductor nanocrystals, suggesting that plasmonic effects may contribute to the IR spectra of these *n*-doped PbSe QDs, too. The localized surface plasmon resonances of colloidal ZnO QDs were demonstrated to be non-classical ("quantum" plasmons), with energies depending on both the classical Drude-type free-carrier resonances as well as on one-electron intraband quantum excitations,[41] and a similar situation can be anticipated for the heavily *n*-doped PbSe QDs investigated here. Indeed, electrochemically charged PbSe QD films show the dominant IR feature blueshifting with charge-carrier injection,[20] consistent with plasmonic behavior.[41]

Given the strong confirmation of the $1P_h$-$1P_e$ band assignment provided by these data, the question then arises whether the formally forbidden $1S_{h,e}$-$1P_{e,h}$ transitions are affected by photodoping in these PbSe QDs. The dipole-forbidden $1S_{h,e}$-$1P_{e,h}$ band has been predicted theoretically[23,42] and reported experimentally based on ultrafast TA[15-16] spectroscopy to reside between the first and second excitonic maxima in the spectra of PbSe QDs, but $1S_{h,e}$-$1P_{e,h}$ absorption has not been unambiguously identified in any static measurement. The inset in Figure 2.1a shows magnified absorption spectra in the region between the $1S_h$-$1S_e$ and $1P_h$-$1P_e$ peaks. Remarkably, these data show a weak but clear absorption band with its maximum at ~0.78 eV emerging from the baseline with increasing photodoping. Linear baseline subtraction highlights the appearance of a distinct new absorption maximum in these data (see Supporting Information, Fig. 2.10). We attribute this weak band to the much-discussed forbidden $1S_{h,e}$-$1P_{e,h}$ transitions. Its appearance upon photodoping is interpreted as reflecting QD symmetry lowering by the electrostatic dipoles established between added $1S_e$ electrons and their charge-compensating surface counter ions. Indeed, computations have suggested that localized charges at PbSe QD surfaces can create sufficient electrostatic fields to mix 1S and 1P wavefunctions, turning on allowedness in these formally electric-dipole-forbidden $1S_{h,e}$-$1P_{e,h}$ transitions.[23] The data here further suggest that symmetry breaking by charging is cumulative, with each added dipole contributing more absorption intensity in the ensemble, despite a presumably random arrangement of counter cations on the QD surfaces.

This $1S_{h,e}$-$1P_{e,h}$ absorption band rests upon an even larger featureless background signal that itself is sometimes attributed to weakly allowed $1S_{h,e}$-$1P_{e,h}$ absorption. Several other interpretations of this background signal have been proposed, but consensus about its origins has not yet been reached. The data here show that photodoping has a qualitatively different effect on

this background than on the resolved $1S_{h,e}$-$1P_{e,h}$ absorption band; instead of growing with photodoping as the resolved $1S_{h,e}$-$1P_{e,h}$ absorption does, this background signal decreases and is mostly eliminated upon photodoping, recovering again completely upon QD reoxidation (Figure 2.1). This behavior, in addition to its different breadth compared to the resolved bandshape of the photodoping-induced absorption, appears inconsistent with assignment of this entire background signal to parity-forbidden $1S_{h,e}$-$1P_{e,h}$ absorption that is already weakly allowed by symmetry-breaking perturbations.[18,43] If interpreted in the same way as the similarly broad mid-gap absorption that appears with photodoping, then this broad absorption that disappears with photodoping would be attributed to trap-state absorption, in this case from electron traps at potentials above the CB edge. Photoexcitation to such traps should occur at energies above the first excitonic transition, and would be eliminated upon raising the Fermi level above these traps. Unfortunately, the dependence of both of the neighboring strong maxima and this background on photodoping precludes any detailed quantitative analysis of the weak but resolved $1S_{h,e}$-$1P_{e,h}$ absorption's dependence on photodoping. Overall, these results emphasize that intensity in the region between the $1S_h$-$1S_e$ and $1P_h$-$1P_e$ bands is only reliably associated with $1S_{h,e}$-$1P_{e,h}$ absorption when there is clear resolution of a discrete absorption band.

In addition to influencing the amplitudes of the PbSe QD absorption features, photodoping also shifts the energies of these features. Figure 2.3a plots the shifts of the $1S_h$-$1S_e$ and $1P_h$-$1P_e$ peaks (ΔE_{SS} and ΔE_{PP}) *vs* $\langle n_{1Se} \rangle$ determined from the d = 6.2 nm QD data in Figure 2.1b. The slope of ΔE_{ss} *vs* $\langle n_{1Se} \rangle$ indicates stabilization of ~1.8 meV/$\langle n_{1Se} \rangle$ for the d = 6.2 nm PbSe QDs. The slope of ΔE *vs* $\langle n_{1Se} \rangle$ is greater for the $1P_h$-$1P_e$ band than for the $1S_h$-$1S_e$ band, reflecting different electrostatic interactions in the two excited states. Similar results are obtained for PbSe QDs of other diameters (see Supporting Information, Fig. 2.11), and reveal a size dependence of the

exciton red shifts. Figure 2.3b,c plots ΔE_{SS} and ΔE_{PP} *vs* $\langle n_{1Se} \rangle$ for d = 7.6, 6.2, and 4.6 nm PbSe QDs, taken from the data in Figures 1 and 2.11. Like the other maxima, the energy of the weak $1S_{h,e}$-$1P_{e,h}$ maximum also appears to decrease with increasing $\langle n_{1Se} \rangle$, but this shift could not be quantified unambiguously because of the low intensities involved.

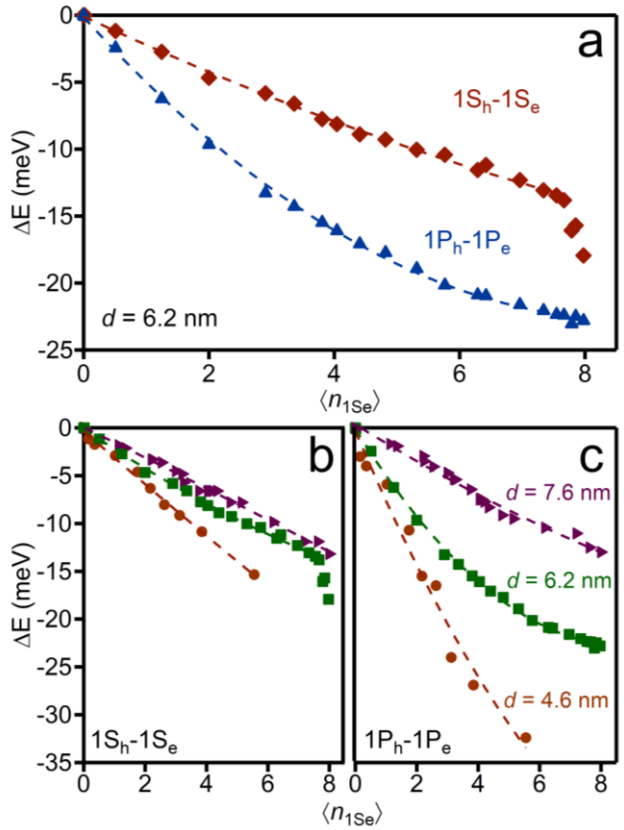

Figure 2.3. (a) Energy shifts of the $1S_h$-$1S_e$ (red diamonds) and $1P_h$-$1P_e$ (blue triangles) excitons as a function of the average number of $1S_e$ electrons per d = 6.2 nm PbSe QD ($\langle n_{1Se} \rangle$). (b) Energy shifts of the $1S_h$-$1S_e$ exciton for d = 7.6 nm (magenta triangles), d = 6.2 nm (green squares), and d = 4.6 (orange circles) nm PbSe QDs plotted as a function of the average number of $1S_e$ electrons per QD ($\langle n_{1Se} \rangle$). (c) Energy shifts of the $1P_h$-$1P_e$ exciton for d = 7.6 nm (magenta triangles), d = 6.2 nm (green squares), and d = 4.6 nm (orange circles) PbSe QDs plotted as a function of the average number of $1S_e$ electrons per QD ($\langle n_{1Se} \rangle$). The dashed lines are guides to the eye.

Qualitatively, these redshifts are entirely consistent with expectations from previous multi- and charged-exciton work. Quantitatively, the data in Figure 2.3a are unexpectedly similar to analogous data for multiexcitons in PbSe QDs measured by TA spectroscopy. For example,

redshifts of ΔE_{SS} = 3 and 6 meV (ΔE_{PP} = 6 and 15 meV) have been reported[14] for d = 6.8 nm PbSe QDs possessing 1 and 4 extra excitons, respectively, compared to ΔE_{SS} = 2.4 and 8.1 meV (ΔE_{PP} = 4.8 and 16 meV) for $\langle n_{1Se} \rangle$ = 1 and 4, respectively, from Figure 2.3a (see Supporting Information, Fig. 2.12). Biexciton redshifts are also greater in d = 3.8 nm PbSe QDs[16] than in d = 6.8 nm PbSe QDs,[14] similar to the exciton size dependence of the photodoped QDs shown in Figures 2.3b,c and 2.13 (see Supporting Information, Fig. 2.14 for TEM images of the different-sized QDs). The nearly identical energies for multiply charged and multiexciton PbSe QDs suggest that the key interactions responsible for stabilizing excitons in both must be the same.

Generally, such redshifts are discussed in terms of pairwise Coulomb interactions between charge carriers, as illustrated in Scheme 2.1a for the simplest-case scenario of $1S_h$-$1S_e$ excitons in the presence of one excess $1S_h$-$1S_e$ exciton or $1S_e$ CB electron. In both photodoped and multiexcitonic QDs, the exciton being formed by absorption interacts with the preexisting charges through Coulomb attraction between opposite charges (J_{eh}, J_{ec}) and repulsion between like charges (J_{ee}, J_{hc}). Exchange (K) provides a quantum-mechanical correction for carrier pairs with like charges and parallel spins, diminishing J_{ee} somewhat. The energy required to create a new exciton in a charged or multiexcitonic QD is modified by the sum of such pairwise interactions relative to an exciton in the same QD without the additional carriers. An exciton redshift indicates that the attractive interactions outweigh the repulsive interactions. For example, exciton redshifts are smaller in multiexcitonic PbSe QDs than in multiexcitonic CdSe QDs, attributable to the fact that PbSe has smaller differences between electron and hole effective masses (delocalization lengths), such that its positive and negative Coulomb interactions cancel each other out almost exactly. Redshifts calculated using a simplified 2D harmonic oscillator model[44] based on PbSe QD single-particle wavefunctions indeed sum to nearly zero, much too small to account for the experimental

multiexciton redshifts. Clearly, this model is incomplete and other factors must make essential contributions to these red shifts.

Scheme 2.1. Comparison of potential mechanisms for exciton stabilization in the multi-carrier configurations of PbSe QDs: (A) Pairwise Coulomb and exchange interactions for multiexcitons (left) and charged excitons (right), (B) Stark effect introduced upon formation of a charged exciton, and (C) electrostatic stabilization by carrier correlation in a charged exciton.

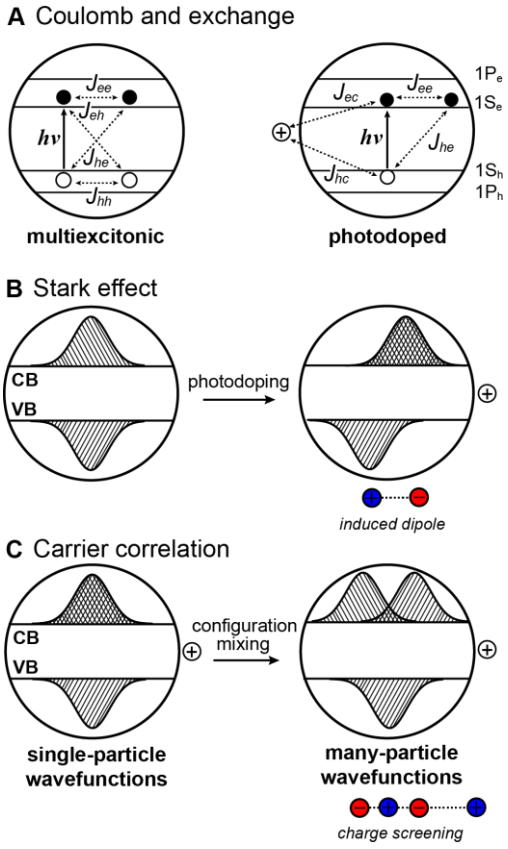

Beyond first-order Coulomb and exchange interactions, two other physical effects could conceivably be responsible for the observed redshifts: Stark effects and carrier correlation. In photodoped QDs, for example, the electric field associated with localization of a positive charge on the QD surface might be expected to perturb the energy of a second core exciton (Scheme

2.1B), analogous to the exciton Stark shifts observed for many QDs subjected to external electric fields. There is no analogous electric field expected for multiexciton configurations involving only core carriers, however, yet the latter show the same redshifts as the charged excitons. This comparison eliminates the Stark effect as the primary source of the energy shifts in Figure 2.3. On the other hand, carrier correlation is expected in both multi- and charged-exciton configurations. Correlation lowers total energies by distorting the single-particle wavefunctions in response to the presence of other carriers (Scheme 2.1C), thereby reducing repulsive inter-carrier Coulomb energies. Such distortion occurs *via* configuration mixing.[45-46] Because of correlation, negative trions assume a spatial charge distribution analogous to that of a hydride ion (Scheme 2.1C), and the spatial charge distribution of a biexciton becomes analogous to that of dihydrogen,[47] rather than each carrier retaining its unperturbed single-particle wavefunction in each scenario. The above discussion leads us to conclude that the multi- and charged-exciton redshifts seen in PbSe QDs are dominated by correlation effects. This conclusion is supported by theoretical predictions that correlation stabilizes biexcitons in d = 8.0 nm CdSe QDs by ~6 meV,[48] a magnitude comparable to the redshifts observed in Figure 2.3. Notably, the first-exciton redshifts of photodoped d = 3.8 nm CdSe QDs[29] and multiexcitonic d = 4.2 nm CdSe QDs[49] are both ~15 meV at one excess electron or exciton, again similar to one another but both nearly 10-fold greater than the 2.4 meV redshift we observe for the first exciton of d = 4.6 nm PbSe QDs (Figure 2.3). The enhanced redshifts in CdSe QDs may reflect greater correlation because of weaker confinement and smaller electrostatic screening in this lattice, and hence a greater imbalance of Coulomb interactions.

2.4 **Summary**

In summary, we report successful photochemical electronic doping of colloidal PbSe QDs. This photodoping differs from previous methods in that it involves UV photolysis of THF to generate radicals that then transfer electrons to the QDs, rather than photoexcitation of the QDs themselves to trigger oxidation of sacrificial reductants. We show that this unique procedure for QD photodoping allows precise control over carrier densities, and that the photodoping can be completely reversed *via* titration with molecular oxidants to return the QDs to their original form, with no evidence of ripening or degradation. A major advantage of this photodoping method over direct chemical reduction is that with this method there is no standing reservoir of reductant in solution along with the doped QDs, allowing redox titration of the accumulated electrons. At maximum photodoping, we observe complete filling of the quantum-confined $1S_e$ CB-edge orbitals, as well as partial population of the higher-energy $1P_e$ orbitals. The high-quality absorption spectra obtained during photodoping and reoxidation permit unambiguous assignment of the long-debated second excitonic absorption maximum to $1P_h$-$1P_e$ excitations. Electrostatic effects from the spectator charges in photodoped QDs also allow direct detection of the formally parity-forbidden $1S_{h,e}$-$1P_{e,h}$ excitations at an energy between the $1S_h$-$1S_e$ and $1P_h$-$1P_e$ maxima. A remarkable quantitative similarity between exciton redshifts in photodoped and multiexciton QDs is observed, despite surface-localized positive charges in the former. The role of charge-carrier correlation in the exciton redshifts of both multi- and charged-exciton configurations is discussed. Overall, these results help to resolve long-standing ambiguities about band assignments in the absorption spectra of PbSe QDs, provide insight into electrostatic multi-carrier effects in these QDs. Although optimized for free-standing PbSe QDs, similar photochemistry may enable facile doping of other colloidal semiconductor nanocrystals (or nanocrystal solids) as well, introducing

new opportunities for preparing and interrogating degenerately *n*-doped semiconductor nanostructures relevant to both fundamental and applied sciences.

2.5 **Experimental Methods**

2.5.1 *General Considerations.*

All syntheses were carried out anaerobically using standard Schlenk line techniques under nitrogen. No difference in the absorption spectra was observed between QDs that were worked up in air and QDs that were worked up anaerobically in a nitrogen glove box. QD samples were stored in a nitrogen glove box.

2.5.2 *Chemicals.*

Unless otherwise noted, all materials were used as-received without further purification. 1-octadecene (ODE, 90%), oleic acid (OA, 90%), selenium powder (100 mesh, 99.99%), and diphenylphosphine (DPP, 98%) were purchased from Sigma-Aldrich. Lead (II) oxide (PbO, 99.999%) was purchased from Alfa Aesar and tri-n-octylphosphine (TOP, ≥ 97%) was purchased from Strem Chemicals. Anhydrous tetrahydrofuran (THF) was purified through columns of dried alumina. Ferrocenium tetrafluoroborate ($FcBF_4$) was prepared from ferrocene and HBF_4OEt_2 (Sigma-Aldrich) following literature procedures.[50]

2.5.3 *Physical Measurements.*

All UV-vis-NIR absorption spectra were collected at room temperature in a Cary 5000 spectrophotometer (Varian). QD concentrations were determined from the energy of the first excitonic peak and the absorbance at 400 nm.[48] Transmission electron microscope (TEM) images

were taken on a FEI Tecnai G2 F20 operating at 200 kV. Infrared (IR) absorption measurements were performed by first photodoping a solution of PbSe QDs in an air-free quartz cuvette. A portion of the solution was then transferred to an air-free IR cell with CaF_2 windows and a 500 μm Teflon spacer in a nitrogen glove box. IR absorption was measured on a Thermo-Scientific Nicolet-8700 spectrometer with a HgCdTe detector.

2.5.4 *PbSe Nanocrystal Synthesis.*

Colloidal PbSe QDs were synthesized using modified literature procedures.[51-53] In a typical synthesis, 0.446 g (2 mmol) of PbO, 1.42 g (5 mmol) of OA and 8.00 g (32 mmol) of ODE were added to a 50 mL 3-neck flask. The mixture was heated to 120 °C with stirring under vacuum for 2 hours. In a 10-mL pear flask, 0.32 g (4 mmol) of Se powder were combined with ~ 4 mL (9 mmol) of TOP in a nitrogen-filled glove box. This mixture was then taken out of the glovebox and placed in a warm ultrasonic bath to form TOP-Se. The Pb-oleate solution was then heated to the desired injection temperature (145 – 200 °C) under nitrogen. Next, 50 μL of diphenylphosphine were injected into the flask, followed immediately by rapid injection of the TOP-Se solution. The temperature was lowered to the desired growth temperature (130 – 180 °C) and the flask was heated for 30 s – 10 minutes, followed by cooling in a water bath. After cooling to room temperature, the QDs were precipitated from solution by addition of acetone and centrifugation. The QDs were then washed by dispersing in hexane and precipitating with acetone twice. Finally, the QDs were dried under nitrogen, pumped into a nitrogen glove box and dispersed in anhydrous THF.

2.5.5 *Photodoping.*

All QD solutions for photodoping were prepared anaerobically in a nitrogen glove box. The QDs were added to a 1 cm quartz cuvette fitted with a Teflon valve and diluted with neat THF. The cuvette was removed from the glove box and its absorption was measured using a Cary 5000 UV-vis-NIR spectrophotometer. Next, the cuvette was irradiated with an Oriel photolysis lamp (200 W Hg/Xe). After irradiating for 1-20 min intervals, the sample was removed from the photolysis beam and its absorption spectrum was re-measured. Longer irradiation is required for more concentrated samples. For example, the QDs in Fig. 1 were fully photodoped after ~110 min of irradiation in 10 min intervals. Photodoping was considered to be complete when the absorption profile did not change between two consecutive photolysis intervals of at least 5 minutes.

2.5.6 *Titration.*

Oxidative titration experiments were performed by adding aliquots of a THF solution of $FcBF_4$ to a THF solution of photodoped PbSe QDs in an air-free cuvette fitted with a Teflon valve. All additions of titrant were performed anaerobically in a nitrogen glove box. First, the concentration of the PbSe QD solution under investigation was determined from its absorbance at 400 nm.[54] Next, the $FcBF_4$ solution was prepared at a concentration such that 0.5 – 1 equivalents of $FcBF_4$ per PbSe QD were added to the cuvette for every 10 μL aliquot of titrant. Aliquots of the titrant were added until the absorption profile fully recovered and did not show a change between sequential additions of titrant. The cuvette was then opened in air and its absorption spectrum remeasured to confirm that all excess electrons had been removed.

2.6 **References**

1. Jiang, X. M.; Schaller, R. D.; Lee, S. B.; Pietryga, J. M.; Klimov, V. I.; Zakhidov, A. A., PbSe nanocrystal/conducting polymer solar cells with an infrared response to 2 micron. *J. Mater. Res.* **2007,** *22*, 2204-2210.
2. Semonin, O. E.; Luther, J. M.; Choi, S.; Chen, H. Y.; Gao, J.; Nozik, A. J.; Beard, M. C., Peak external photocurrent quantum efficiency exceeding 100% via MEG in a quantum dot solar cell. *Science* **2011,** *334*, 1530-3.
3. Zhang, J.; Gao, J.; Church, C. P.; Miller, E. M.; Luther, J. M.; Klimov, V. I.; Beard, M. C., PbSe quantum dot solar cells with more than 6% efficiency fabricated in ambient atmosphere. *Nano Lett* **2014,** *14*, 6010-5.
4. Kim, S.; Marshall, A. R.; Kroupa, D. M.; Miller, E. M.; Luther, J. M.; Jeong, S.; Beard, M. C., Air-Stable and Efficient PbSe Quantum-Dot Solar Cells Based upon ZnSe to PbSe Cation-Exchanged Quantum Dots. *ACS Nano* **2015,** *9*, 8157-8164.
5. Marshall, A. R.; Young, M. R.; Nozik, A. J.; Beard, M. C.; Luther, J. M., Exploration of Metal Chloride Uptake for Improved Performance Characteristics of PbSe Quantum Dot Solar Cells. *J. Phys. Chem. Let.* **2015**, 2892-2899.
6. Prins, F.; Buscema, M.; Seldenthuis, J. S.; Etaki, S.; Buchs, G.; Barkelid, M.; Zwiller, V.; Gao, Y.; Houtepen, A. J.; Siebbeles, L. D.; van der Zant, H. S., Fast and efficient photodetection in nanoscale quantum-dot junctions. *Nano Lett.* **2012,** *12*, 5740-3.
7. Ellingson, R. J.; Beard, M. C.; Johnson, J. C.; Yu, P.; Micic, O. I.; Nozik, A. J.; Shabaev, A.; Efros, A. L., Highly efficient multiple exciton generation in colloidal PbSe and PbS quantum dots. *Nano Lett.* **2005,** *5*, 865-71.
8. Gdor, I.; Sachs, H.; Roitblat, A.; Strasfeld, D. B.; Bawendi, M. G.; Ruhman, S., Exploring exciton relaxation and multiexciton generation in PbSe nanocrystals using hyperspectral near-IR probing. *ACS Nano* **2012,** *6*, 3269-77.
9. Spoor, F. C.; Kunneman, L. T.; Evers, W. H.; Renaud, N.; Grozema, F. C.; Houtepen, A. J.; Siebbeles, L. D., Hole Cooling Is Much Faster than Electron Cooling in PbSe Quantum Dots. *ACS Nano* **2016,** *10*, 695-703.
10. Wehrenberg, B. L.; Wang, C. J.; Guyot-Sionnest, P., Interband and intraband optical studies of PbSe colloidal quantum dots. *J. Phys. Chem. B* **2002,** *106*, 10634-10640.
11. Allan, G.; Delerue, C., Confinement effects in PbSe quantum wells and nanocrystals. *Phys. Rev. B* **2004,** *70*, 245321.
12. Peterson, J. J.; Huang, L.; Delerue, C.; Allan, G.; Krauss, T. D., Uncovering forbidden optical transitions in PbSe nanocrystals. *Nano Lett.* **2007,** *7*, 3827-31.
13. Liljeroth, P.; Zeijlmans van Emmichoven, P. A.; Hickey, S. G.; Weller, H.; Grandidier, B.; Allan, G.; Vanmaekelbergh, D., Density of states measured by scanning-tunneling spectroscopy sheds new light on the optical transitions in PbSe nanocrystals. *Phys. Rev. Lett.* **2005,** *95*, 086801.
14. Trinh, M. T.; Houtepen, A. J.; Schins, J. M.; Piris, J.; Siebbeles, L. D., Nature of the second optical transition in PbSe nanocrystals. *Nano Lett.* **2008,** *8*, 2112-7.
15. Schins, J. M.; Trinh, M. T.; Houtepen, A. J.; Siebbeles, L. D. A., Probing formally forbidden optical transitions in PbSe nanocrystals by time- and energy-resolved transient absorption spectroscopy. *Phys. Rev. B* **2009,** *80*, 035323.
16. Trinh, M. T.; Sfeir, M. Y.; Choi, J. J.; Owen, J. S.; Zhu, X., A hot electron-hole pair breaks the symmetry of a semiconductor quantum dot. *Nano Lett.* **2013,** *13*, 6091-7.

17. Koole, R.; Allan, G.; Delerue, C.; Meijerink, A.; Vanmaekelbergh, D.; Houtepen, A. J., Optical investigation of quantum confinement in PbSe nanocrystals at different points in the Brillouin zone. *Small* **2008,** *4*, 127-33.
18. Moreels, I.; Hens, Z., On the interpretation of colloidal quantum-dot absorption spectra. *Small* **2008,** *4*, 1866-1868.
19. Koh, W. K.; Koposov, A. Y.; Stewart, J. T.; Pal, B. N.; Robel, I.; Pietryga, J. M.; Klimov, V. I., Heavily doped n-type PbSe and PbS nanocrystals using ground-state charge transfer from cobaltocene. *Sci. Rep.* **2013,** *3*, 2004.
20. Wehrenberg, B. L.; Guyot-Sionnest, P., Electron and hole injection in PbSe quantum dot films. *J. Am. Chem. Soc.* **2003,** *125*, 7806-7.
21. Kroupa, D. M.; Hughes, B. K.; Miller, E. M.; Moore, D. T.; Anderson, N. C.; Chernomordik, B. D.; Nozik, A. J.; Beard, M. C., Synthesis and Spectroscopy of Silver-Doped PbSe Quantum Dots. *J. Am. Chem. Soc.* **2017,** *139*, 10382-10394.
22. Alimoradi Jazi, M.; Janssen, V.; Evers, W. H.; Tadjine, A.; Delerue, C.; Siebbeles, L. D. A.; van der Zant, H. S. J.; Houtepen, A. J.; Vanmaekelbergh, D., Transport Properties of a Two-Dimensional PbSe Square Superstructure in an Electrolyte-Gated Transistor. *Nano Lett.* **2017,** *17*, 5238-5243.
23. An, J. M.; Franceschetti, A.; Zunger, A., Pauli blocking versus electrostatic attenuation of optical transition intensities in charged PbSe quantum dots. *Phys. Rev. B* **2007,** *76*, 161310.
24. Haase, M.; Weller, H.; Henglein, A., Photochemistry and radiation chemistry of colloidal semiconductors. 23. Electron storage on zinc oxide particles and size quantization. *J. Phys. Chem.* **1988,** *92*, 482-487.
25. Wood, A.; Giersig, M.; Mulvaney, P., Fermi level equilibration in quantum dot-metal nanojunctions. *J. Phys. Chem. B* **2001,** *105*, 8810-8815.
26. Shim, M.; Guyot-Sionnest, P., Organic-capped ZnO nanocrystals: synthesis and n-type character. *J. Am. Chem. Soc.* **2001,** *123*, 11651-4.
27. Liu, W. K.; Whitaker, K. M.; Smith, A. L.; Kittilstved, K. R.; Robinson, B. H.; Gamelin, D. R., Room-temperature electron spin dynamics in free-standing ZnO quantum dots. *Phys. Rev. Lett.* **2007,** *98*, 186804.
28. Schimpf, A. M.; Gunthardt, C. E.; Rinehart, J. D.; Mayer, J. M.; Gamelin, D. R., Controlling carrier densities in photochemically reduced colloidal ZnO nanocrystals: Size dependence and role of the hole quencher. *J. Am. Chem. Soc.* **2013,** *135*, 16569-16577.
29. Rinehart, J. D.; Schimpf, A. M.; Weaver, A. L.; Cohn, A. W.; Gamelin, D. R., Photochemical electronic doping of colloidal CdSe nanocrystals. *J. Am. Chem. Soc.* **2013,** *135*, 18782-5.
30. Tsui, E. Y.; Hartstein, K. H.; Gamelin, D. R., Selenium Redox Reactivity on Colloidal CdSe Quantum Dot Surfaces. *J. Am. Chem. Soc.* **2016,** *138*, 11105-8.
31. Tsui, E. Y.; Carroll, G. M.; Miller, B.; Marchioro, A.; Gamelin, D. R., Extremely Slow Spontaneous Electron Trapping in Photodoped n-Type CdSe Nanocrystals. *Chem. Mater.* **2017,** *29*, 3754-3762.
32. Cohn, A. W.; Rinehart, J. D.; Schimpf, A. M.; Weaver, A. L.; Gamelin, D. R., Size dependence of negative trion Auger recombination in photodoped CdSe nanocrystals. *Nano Lett.*. **2014,** *14*, 353-8.
33. Cohn, A. W.; Schimpf, A. M.; Gunthardt, C. E.; Gamelin, D. R., Size-dependent trap-assisted auger recombination in semiconductor nanocrystals. *Nano Lett.* **2013,** *13*, 1810-1815.

34. Carroll, G. M.; Brozek, C. K.; Hartstein, K. H.; Tsui, E. Y.; Gamelin, D. R., Potentiometric Measurements of Semiconductor Nanocrystal Redox Potentials. *J. Am. Chem. Soc.* **2016,** *138*, 4310-3.
35. Carroll, G. M.; Schimpf, A. M.; Tsui, E. Y.; Gamelin, D. R., Redox Potentials of Colloidal n-Type ZnO Nanocrystals: Effects of Confinement, Electron Density, and Fermi-Level Pinning by Aldehyde Hydrogenation. *J. Am. Chem. Soc.* **2015,** *137*, 11163-9.
36. Carroll, G. M.; Tsui, E. Y.; Brozek, C. K.; Gamelin, D. R., Spectroelectrochemical Measurement of Surface Electrostatic Contributions to Colloidal CdSe Nanocrystal Redox Potentials. *Chem. Mater.* **2016,** *28*, 7912-7918.
37. Lee, S. H., Dynamics of multi-channel dissociation of tetrahydrofuran photoexcited at 193 nm: distributions of kinetic energy, angular anisotropies and branching ratios. *Phys. Chem. Chem. Phys.* **2010,** *12*, 2655-63.
38. Ishida, A.; Sugita, D.; Takamuku, S., Photoinduced Formation and Reaction of Benzalaniline Radical-Anions - Comparison with the Radiation-Induced Reaction. *J Photoch. Photobio. A* **1992,** *65*, 197-204.
39. An, J. M.; Franceschetti, A.; Dudiy, S. V.; Zunger, A., The peculiar electronic structure of PbSe quantum dots. *Nano Lett.* **2006,** *6*, 2728-35.
40. Liu, H. B.; Brozek, C. K.; Sun, S. C.; Lingerfelt, D. B.; Gamelin, D. R.; Li, X. S., A Hybrid Quantum-Classical Model of Electrostatics in Multiply Charged Quantum Dots. *J. Phys. Chem. C* **2017,** *121*, 26086-26095.
41. Schimpf, A. M.; Thakkar, N.; Gunthardt, C. E.; Masiello, D. J.; Gamelin, D. R., Charge-tunable quantum plasmons in colloidal semiconductor nanocrystals. *ACS Nano* **2014,** *8*, 1065-72.
42. Franceschetti, A.; Luo, J. W.; An, J. M.; Zunger, A., Origin of one-photon and two-photon optical transitions in PbSe nanocrystals. *Phys. Rev. B* **2009,** *79*, 241311.
43. Kilina, S. V.; Kilin, D. S.; Prezhdo, O. V., Breaking the phonon bottleneck in PbSe and CdSe quantum dots: time-domain density functional theory of charge carrier relaxation. *ACS Nano* **2009,** *3*, 93-9.
44. Warburton, R. J.; Miller, B. T.; Durr, C. S.; Bodefeld, C.; Karrai, K.; Kotthaus, J. P.; Medeiros-Ribeiro, G.; Petroff, P. M.; Huant, S., Coulomb interactions in small charge-tunable quantum dots: A simple model. *Phys. Rev. B* **1998,** *58*, 16221-16231.
45. Banyard, K. E., Electron Correlation in Atoms and Molecules. *J. Chem. Educ.* **1970,** *47*, 668-671.
46. Dunbar, R. C., The Influence of Electrons on Each Other in a Molecule: Correlation of Electron Motions in H_2. *J. Chem. Educ.* **1989,** *66*, 463-466.
47. Riva, C.; Peeters, F. M.; Varga, K.; Schweigert, V. A., Correlation energy and configuration of biexcitons in quantum wells. *Phys. Status Solidi B-Basic Res.* **2002,** *234*, 50-57.
48. Shumway, J.; Franceschetti, A.; Zunger, A., Correlation versus mean-field contributions to excitons, multiexcitons, and charging energies in semiconductor quantum dots. *Phys. Rev. B* **2001,** *63*, 155316.
49. Sewall, S. L.; Franceschetti, A.; Cooney, R. R.; Zunger, A.; Kambhampati, P., Direct observation of the structure of band-edge biexcitons in colloidal semiconductor CdSe quantum dots. *Phys. Rev. B* **2009,** *80*, 081310.
50. Connelly, N. G.; Geiger, W. E., Chemical Redox Agents for Organometallic Chemistry. *Chem. Rev.* **1996,** *96*, 877-910.

51. Yu, W. W.; Falkner, J. C.; Shih, B. S.; Colvin, V. L., Preparation and characterization of monodisperse PbSe semiconductor nanocrystals in a noncoordinating solvent. *Chem. Mater.* **2004,** *16,* 3318-3322.
52. Shapiro, A.; Jang, Y. J.; Rubin-Brusilovski, A.; Budniak, A. K.; Horani, F.; Sashchiuk, A.; Lifshitz, E., Tuning Optical Activity of IV-VI Colloidal Quantum Dots in the Short-Wave Infrared (SWIR) Spectral Regime. *Chem. Mater.* **2016,** *28,* 6409-6416.
53. Steckel, J. S.; Yen, B. K.; Oertel, D. C.; Bawendi, M. G., On the mechanism of lead chalcogenide nanocrystal formation. *J. Am. Chem. Soc.* **2006,** *128,* 13032-3.
54. Moreels, I.; Lambert, K.; De Muynck, D.; Vanhaecke, F.; Poelman, D.; Martins, J. C.; Allan, G.; Hens, Z., Composition and size-dependent extinction coefficient of colloidal PbSe quantum dots. *Chem. Mater.* **2007,** *19,* 6101-6106.

2.7 **Supporting Information**

THF Photolysis

THF will decompose upon UV irradiation, forming many organic fragments including radical and diradical species.[1-2] One possible dissociation pathway is:

$$C_4H_8O \rightarrow H\bullet + CH_2CH_2CH_2(C\bullet)HO$$

The unpaired electrons in the radical intermediates can be located on carbon, oxygen, or hydrogen atoms. The data in the main text are interpreted as indicating that such radicals reduce PbSe QDs, similar to the photochemical reactions between THF and organic molecules.[38] Reduced QDs need to have cations at their surfaces for charge compensation, therefore the radical species considered most likely to reduce the QDs is H•, resulting in:

$$H\bullet + PbSe \rightarrow e^-_{CB}:PbSe\text{-}H^+$$

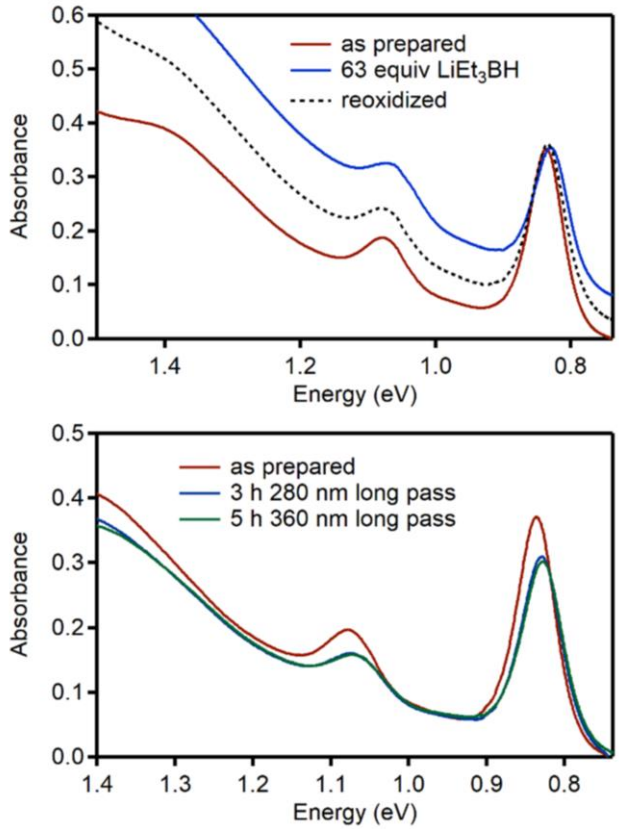

Figure 2.4. (Top) Absorption spectra of a THF solution of d = 4.7 nm PbSe QDs before (red) and after the addition of 63 equivalents Li[Et_3BH] (blue). The black dotted line shows the spectrum after exposing the solution to air. (Bottom) Absorption spectra of a THF solution of d = 4.7 nm PbSe QDs. The solution was irradiated for three hours using a 280 nm long-pass filter (blue) followed by irradiation for five hours using a 360 nm long pass filter (green).

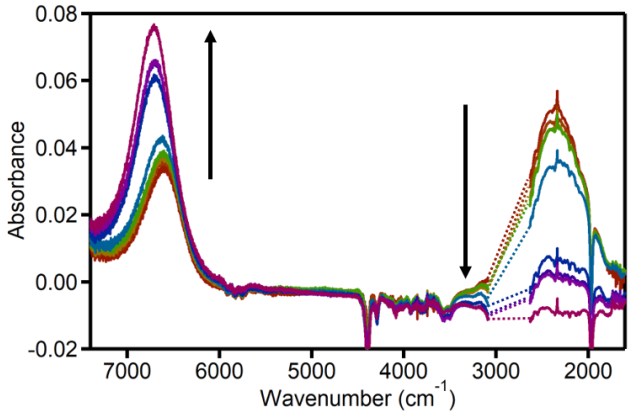

Figure 2.5. Infrared absorption spectra of d = 4.7 nm PbSe QDs that are partially photodoped (red) and re-oxidized in air (pink), as well as at various intermediate stages of re-oxidation. The arrows show the direction of excitonic absorption bleach recovery (~6700 cm^{-1}) and the decrease of low-energy intraband absorption (~2350 cm^{-1}) as the sample is oxidized.

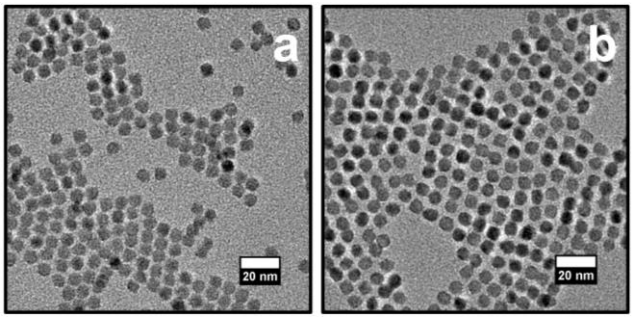

Figure 2.6. TEM images of d = 7.6 nm PbSe QDs before (a) and after (b) photodoping in THF. The QDs in panel b were reoxidized by titration with $FcBF_4$. The scale bars are 20 nm.

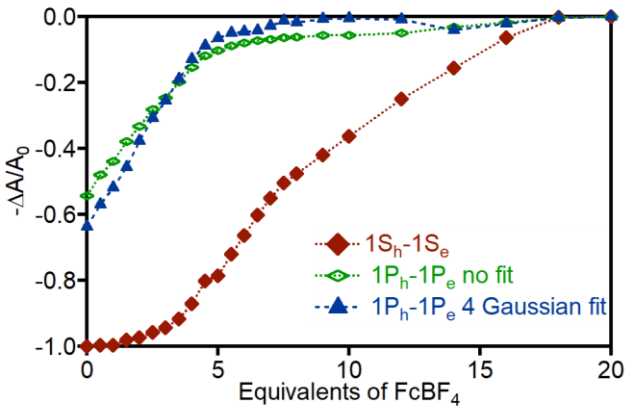

Figure 2.7. Normalized differential absorbance of the $1S_h$-$1S_e$ and $1P_h$-$1P_e$ excitonic transitions of d = 6.2 nm PbSe QDs plotted *vs* equivalents of oxidant added to the fully photodoped QD sample. The green symbols plot $1P_h$-$1P_e$ amplitudes obtained simply by estimating the baseline and quantifying the peak amplitude, with no fitting. The blue triangles plot $1P_h$-$1P_e$ amplitudes obtained by fitting the low-energy portion of the absorption spectrum to the sum of four Gaussians. Both curves lead to the same conclusions, demonstrating that the conclusions drawn from these data in the main text are independent of the analysis method. The $1S_h$-$1S_e$ transition also gives the same result regardless of the analysis procedure.

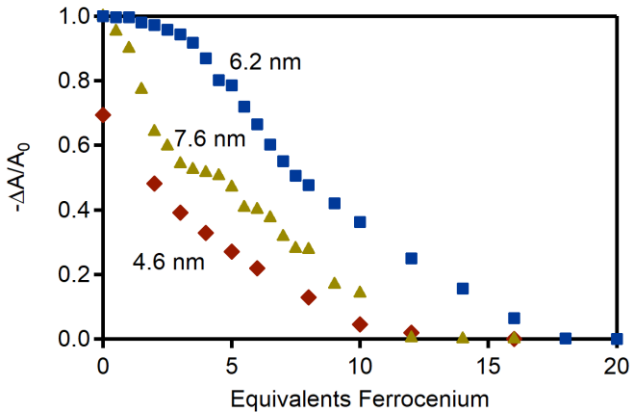

Figure 2.8. Normalized differential absorption measured at the $1S_h$-$1S_e$ exciton of maximally photodoped PbSe QDs of different diameters, plotted as a function of added equivalents of oxidant. $FcBF_4$ was used as the oxidant for the d = 6.2 and d = 7.6 nm QDs. FcOTf was used for the d = 4.6 nm QDs.

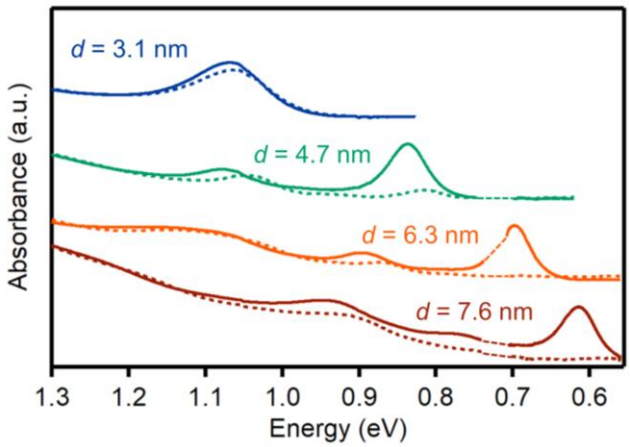

Figure 2.9. Size dependence of the absorption spectra of PbSe QDs collected before (solid lines) and after (dashed lines) maximal photodoping. The energy regions with intense solvent C-H stretches (0.707-0.737 eV) have been interpolated with dotted lines for clarity.

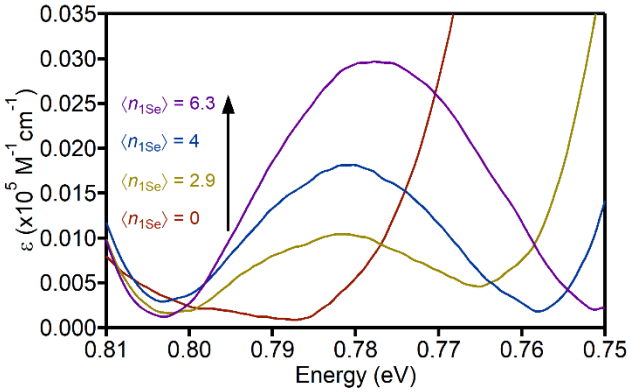

Figure 2.10. Expanded plot of the absorption spectra of d = 6.2 nm PbSe QDs in the region between the $1S_h$-$1S_e$ and $1P_h$-$1P_e$ excitonic peaks, shown for various values of $\langle n_{1Se} \rangle$ and after the subtraction of linear baselines for each. The linear baselines were determined by drawing lines between the inflection points of the absorption spectra from Figure 2.1a, inset.

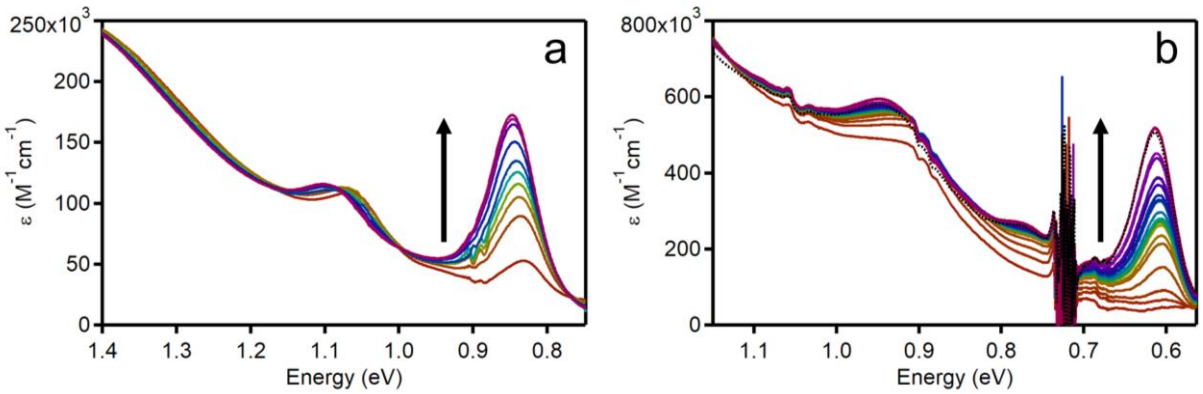

Figure 2.11. Absorption spectra of maximally photodoped **(a)** d = 4.6 nm and **(b)** d = 7.6 nm PbSe QDs collected during titration with FcOTf (4.6 nm QDs) or $FcBF_4$ (7.6 nm QDs). Absorbance is represented as nanocrystal molar extinction coefficient, $M^{-1}cm^{-1}$. The arrows indicate the direction of increasing oxidizing equivalents.

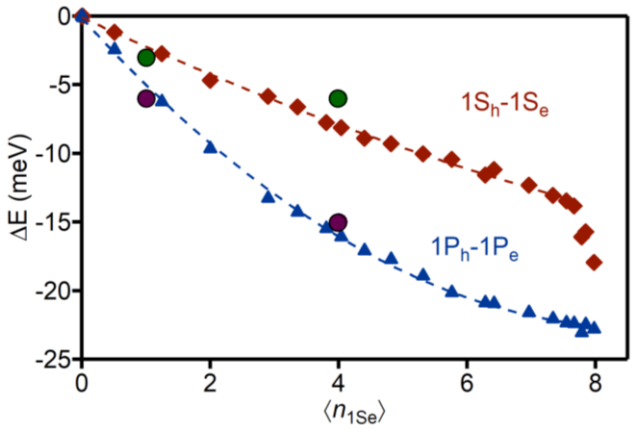

Figure 2.12. Energy shifts of the $1S_h$-$1S_e$ (red diamonds) and $1P_h$-$1P_e$ (blue triangles) excitons as a function of the average number of $1S_e$ electrons per d = 6.2 nm PbSe QD ($\langle n_{1Se} \rangle$). Also shown are the shifts of the $1S_h$-$1S_e$ (black and green circles) and $1P_h$-$1P_e$ (black and purple circles) excitons in d = 6.8 nm PbSe QDs already containing one or four additional excitons, measured by transient absorption.[3] Transient absorption data are adapted from ref. 14.

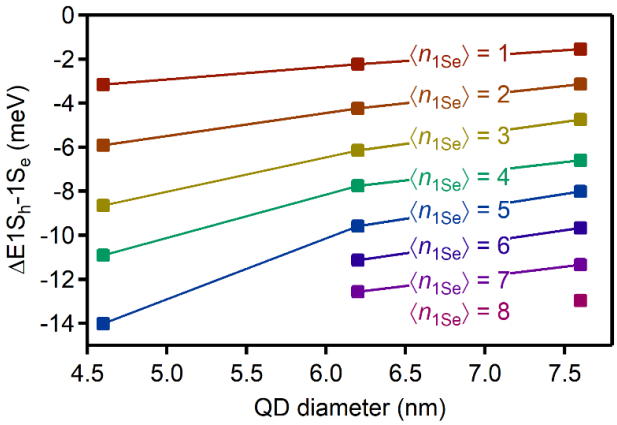

Figure 2.13. Plots of the $1S_h$-$1S_e$ exciton energy shift *vs* QD diameter for different values of $\langle n_{1Se} \rangle$.

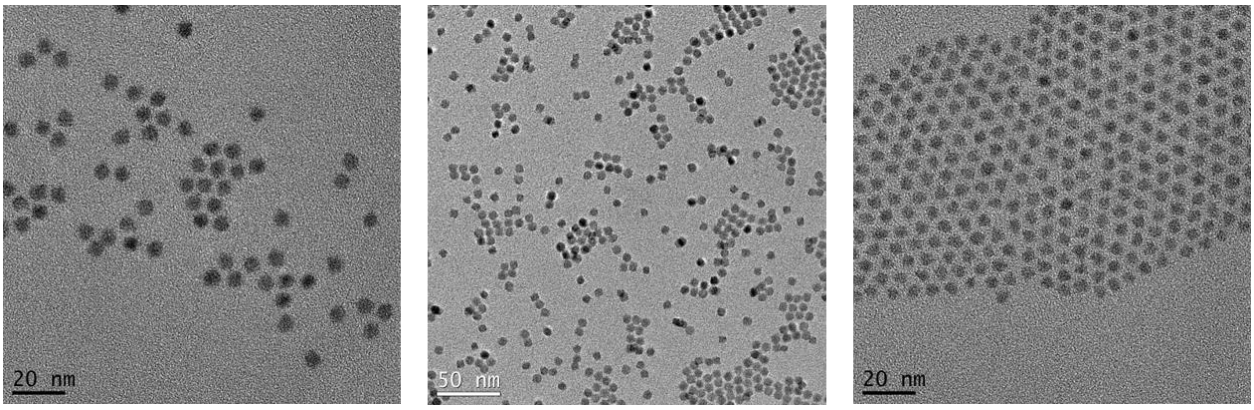

Figure 2.14. TEM images of the (left) 6.2 nm, (middle) 7.6 nm, and (right) 4.6 nm diameter PbSe QDs from the main text (diameters determined by absorption spectroscopy).

References

1. Ishida, A.; Sugita, D.; Takamuku, S., Photoinduced Formation and Reaction of Benzalaniline Radical-Anions - Comparison with the Radiation-Induced Reaction. *J Photoch. Photobio. A* **1992,** *65*, 197-204.
2. Lee, S. H., Dynamics of multi-channel dissociation of tetrahydrofuran photoexcited at 193 nm: distributions of kinetic energy, angular anisotropies and branching ratios. *Phys. Chem. Chem. Phys.* **2010,** *12*, 2655-63.
3. Trinh, M. T.; Houtepen, A. J.; Schins, J. M.; Piris, J.; Siebbeles, L. D., Nature of the second optical transition in PbSe nanocrystals. *Nano Lett.* **2008,** *8*, 2112-7.

Chapter 3. Band-Edge Engineering in Aliovalently Doped Metal-Oxide Nanocrystals

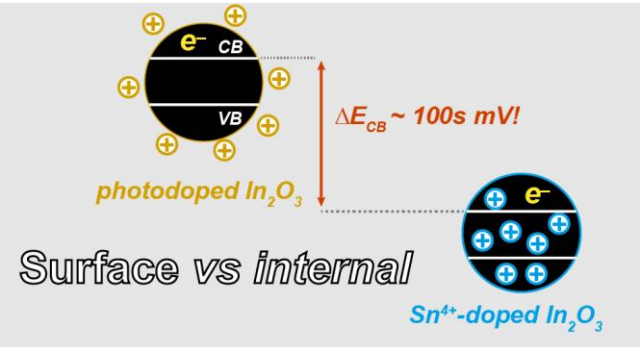

3.1 **Overview**

Degenerately doped metal-oxide nanocrystals (NCs) are attractive for optoelectronic applications because their localized surface plasmon resonances (LSPRs) are tunable *via* their tunable excess charge-carrier densities. The addition of delocalized conduction band (CB) electrons can be achieved through aliovalent doping or by post-synthetic techniques such as photodoping. Here, we examine the role of charge-compensating cations on the redox properties of excess electrons in free-standing colloids of degenerately doped oxide NCs both experimentally and through modeling. Taking Sn^{4+}:In_2O_3 (ITO) NCs as a model system, we use spectroelectrochemical techniques to illustrate a key difference between aliovalent doping and photochemical doping. Whereas photodoping introduces excess CB electrons by raising the Fermi level relative to the CB, aliovalent impurity substitution introduces excess CB electrons by stabilizing the CB relative to the Fermi level. A significant difference is thus observed electrochemically between delocalized CB electrons compensated by aliovalent dopants and those compensated by surface cations (protons). Spectroelectrochemical titrations allow the band-edge

stabilization as a function of Sn^{4+} doping to be quantified. Theoretical modeling illustrates the very different potentials that arise from charge compensation *via* aliovalent substitution and surface charge compensation, both in the total stabilization and in its spatial distribution. These results highlight the role of charge compensation in determining the chemical and physical properties of degenerately doped semiconductor NCs.

3.2 **Introduction**

Degenerately doped semiconductor nanocrystals (NCs) have attracted considerable attention for their tunable electronic and optoelectronic properties.[1-7] Doped metal-oxide NCs such as Al^{3+}:ZnO (AZO),[8-9] Sn^{4+}:In_2O_3 (ITO),[6,10-11] and In^{3+}:CdO (ICO),[12-13] have become particularly attractive for their tunable localized surface plasmon resonances (LSPRs).[4,7,14] Both the LSPR absorption magnitude and its energy can be tuned throughout the near-IR in this class of materials because of their tunable charge-carrier densities, accessed variously through aliovalent doping,[8-10,15] electrochemical charging,[16-17] photodoping,[10,18] and redox chemistry.[19-21] A thorough fundamental understanding of the properties of electrons introduced through these methods is necessary for implementation of next-generation technologies based on degenerately doped semiconductor NCs.

Charge compensation plays a major role in determining the redox characteristics of excess charge carriers in semiconductor NCs. In electrochemical charging, photodoping, or chemical reduction/oxidation, a change in electrochemical potential (Fermi level) relative to a fixed band-edge potential causes carrier transfer into or out of the NC. In aliovalent doping, however, the situation is reversed; aliovalent impurities shift the NC band-edge potentials relative to the Fermi level, resulting in carrier injection from some fixed redox reservoir.[1] In the former case, excess

charges are compensated by counterions at the surface, whereas in the latter excess charges are compensated inside the NC lattice. As a consequence of this difference, for example, the reactivities of ZnO NC conduction-band (CB) electrons added *via* aliovalent doping (*e.g.*, Al^{3+} in AZO NCs) are strikingly different from those of electrons added *via* photodoping.[8] Density functional theory (DFT) calculations show very large CB stabilization by the substitutional Al^{3+}.[22] Even in photodoping or molecular electron transfer, where charge-compensating ions reside at the NC surfaces, the properties of the excess electrons are very sensitive to changes in the steric bulk of the charge-compensating ion.[23-24] Electrostatic modeling describes a strong dependence of carrier potentials on the separation between counter ions and the NC surfaces.[25-26] Recently, spectroelectrochemical measurements have allowed the stabilization energy of valence-band (VB) holes compensated by lattice vacancies in $Cu_{2-x}S$ NCs compared to holes stabilized by surface anions to be analyzed quantitatively,[27] revealing a remarkable ~500 mV difference between these two motifs at equal carrier densities. Despite the anticipation of comparably large band-edge shifts in metal-oxide NCs, the stabilization of CB electrons by aliovalent dopants has not been directly measured for this important class of materials.

Here, we report spectroelectrochemical measurements of degenerately doped metal-oxide NCs. ITO NCs were selected as a model system because of their facile and highly controllable synthesis. Titration of CB electrons from photodoped ITO NCs provides a direct experimental measurement of NC electron densities, facilitating quantitative analysis. *In situ* potentiometric data collected during such titrations further reveal large capacitance values for these NCs. Increasing the Sn^{4+} doping level leads to greater carrier densities (*n* doping), as reported previously, and these spectroelectrochemical measurements further demonstrate that the role of the aliovalent dopants is to dramatically stabilize the CB edge, as opposed to raising the Fermi level. Aliovalent doping

thus allows NC redox-potential tuning. These experimental results are supplemented by theoretical analysis using the charged-sphere model. This model shows that CB electrons are more strongly stabilized inside the NC when their charge-compensating counter ions are located within the NC lattice as aliovalent dopants than when they are located at the NC surfaces.

3.3 **Results and Analysis**

In_2O_3 NCs were synthesized with varying Sn^{4+} content following literature procedures.[6,15] Figure 3.1a shows absorption spectra of In_2O_3 and ITO NCs of varying Sn^{4+} concentration. An intense localized surface plasmon resonance (LSPR) is observed in the near infrared (NIR) of all ITO NC samples, shifting to higher energy as more Sn^{4+} is incorporated, consistent with electronic doping from the addition of Sn^{4+}. A small amount of NIR absorption is also observed even in the undoped In_2O_3 NCs, potentially from free electrons associated with native oxygen vacancies.[28-29] TEM analysis (Fig. 3.1b–e) shows that these NCs range between 12 and 15 nm in diameter. As seen in these images, the introduction of Sn^{4+} influences the NC faceting. For the purposes of this report, the 0.85% ITO NCs were considered cubes and the other NC samples were approximated as spheres.

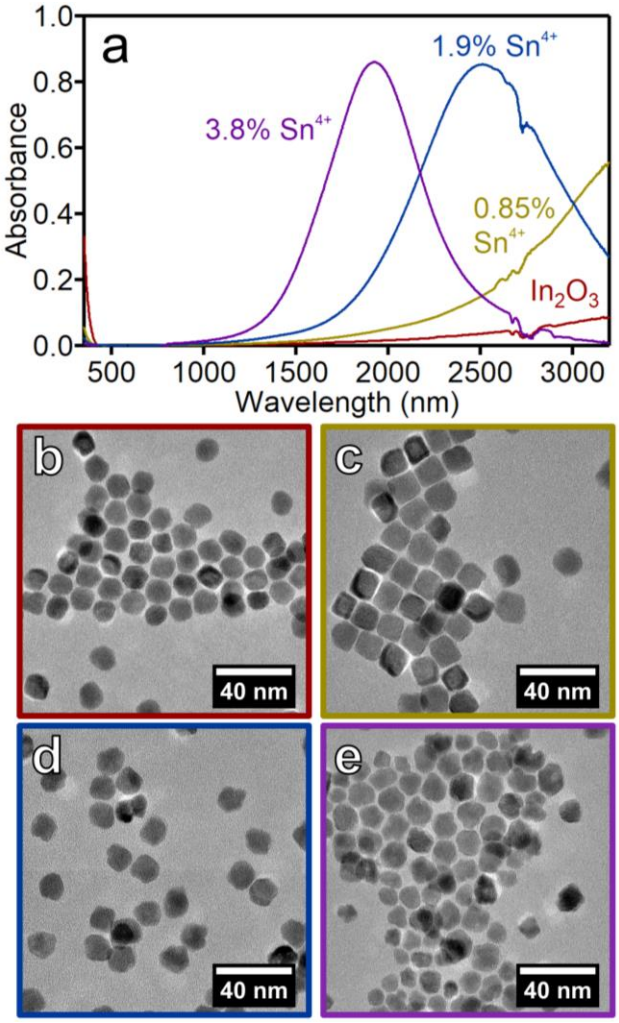

Figure 3.1. (a) Room-temperature absorption spectra of d = 13.1 nm In_2O_3 (red), d = 13.4 nm 0.85% ITO (gold), d = 14.1 nm 1.9% ITO (blue), and d = 12.6 nm 3.8% ITO (purple) nanocrystals. The spectra were measured using tetrachloroethylene as the solvent. Panels (b), (c), (d), and (e) show TEM micrographs of the undoped In_2O_3, 0.85%, 1.9%, and 3.8% Sn^{4+}-doped In_2O_3 (ITO) NCs, respectively.

Figure 3.2 summarizes absorption data from a representative spectroelectrochemical potentiometry experiment performed on ITO NCs (see Experimental section for details). The sample was first photodoped until the absorption stopped increasing and V_{OC} stopped changing. Then, the solution was titrated with aliquots of $FcBF_4$ in 0.1 M $TBAPF_6$/THF. The LSPR absorption decreased as $FcBF_4$ was added, until the as-prepared spectrum was recovered (Fig.

3.2a), consistent with removal of the electrons introduced by photodoping (e^-_{photo}). Further additions of $FcBF_4$ resulted in a further decrease of the plasmon absorption, indicating removal of some of the electrons compensated by the aliovalent dopants (e^-_{alio}). Eventually, the spectra stop changing with the addition of more $FcBF_4$, indicating that e^-_{alio} can no longer be removed from the NCs. By plotting the ratio of the NIR absorbance at 1300 nm (similar results are obtained for other monitoring wavelengths) to the absorbance of the as-prepared solution at the same wavelength (*i.e.*, A/A_0) against equivalents of $FcBF_4$ added per NC (Fig. 3.2b), the data can be analyzed quantitatively.[10]

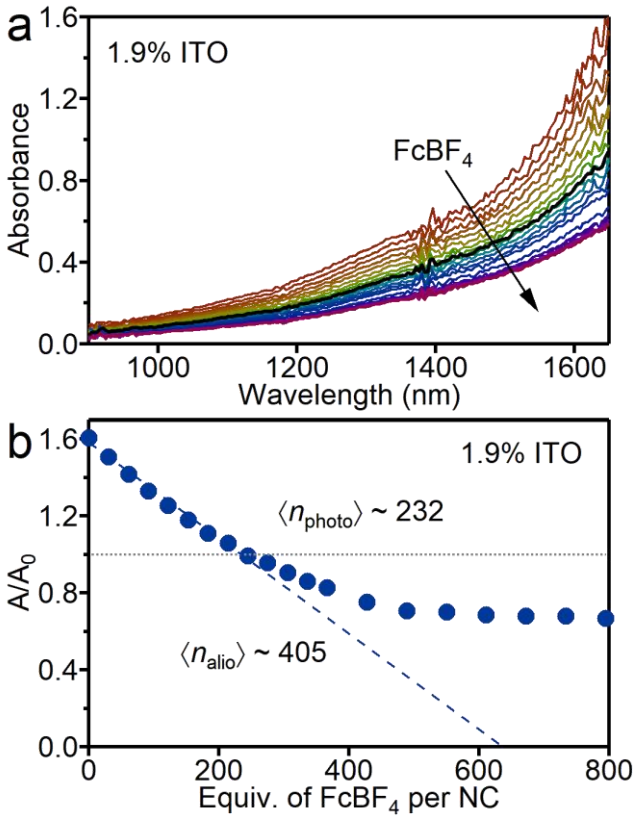

Figure 3.2. (a) Absorption spectra of a solution of maximally photodoped d = 14.1 nm ITO NCs containing 1.9% Sn^{4+}, collected at various stages during oxidative titration with FcBF4. The NCs were suspended in in 0.1 M $TBAPF_6$/THF. The arrow shows the direction of increasing oxidative equivalents. The black spectrum is the absorbance of the as-prepared solution. (b) The ratio of the absorbance at 1300 nm to the absorbance of the as-prepared solution at the same wavelength (A/A_0), plotted against equivalents of $FcBF_4$ added to the maximally photodoped NCs from panel (a). The gray dashed line at A/A_0 = 1

represents the absorption of the as-prepared solution. The dashed blue line is a fit to the data for values of A/A_0 greater than 1 and is extrapolated to $A/A_0 = 0$.

As shown in Figure 3.2b, A/A_0 decreases linearly with the addition of $FcBF_4$ for values of $A/A_0 > 1$, consistent with removal of one electron per equivalent of $FcBF_4$ added. The dashed blue line is a linear fit to this portion of the data. The intersection of this fitted line with $A/A_0 = 1$ indicates the average number of CB electrons per NC added *via* photodoping ($\langle n_{photo} \rangle \sim 232$), and extrapolation of this line to $A/A_0 = 0$ gives an estimate of the total number of CB electrons per NC ($\langle n_{total} \rangle \sim 637$) at maximum photodoping. The average number of CB electrons compensated by aliovalent dopants ($\langle n_{alio} \rangle \sim 405$) in the as-prepared NCs is determined by subtracting $\langle n_{photo} \rangle$ from $\langle n_{total} \rangle$. ICP analysis shows that this 1.9% ITO NC sample contains ~880 Sn^{4+} cations per NC on average, but the titration data suggest only 405 excess CB electrons per NC, indicating that not all Sn^{4+} dopants are accompanied by excess CB electrons (only 46%). For $A/A_0 < 1$, the titration data are no longer linear and they plateau at $A/A_0 \approx 0.68$, suggesting that ~ 32% of $\langle n_{alio} \rangle$ (~130 e^-/NC) can be removed by titration with $FcBF_4$. The same analysis was performed on photodoped In_2O_3, 0.85% ITO, and 3.8% ITO NCs (Supporting Information, Figures 3.7–3.9). The average electron density added to these NCs by maximum photodoping ($\langle N_{photo} \rangle \sim 1.5 \times 10^{20}$ cm^{-3}) is independent of Sn^{4+} concentration (Supporting Information, Figure 3.10), consistent with our previous observations for photodoped ITO NCs.[10]

Figure 3.3 summarizes potentiometric titration data for the entire series of NCs shown in Figure 3.1. The data are plotted as Fermi level *vs* equivalents of $FcBF_4$ added per NC (E_F, in *V vs* $Fc^{+/0}$), starting from the maximally photodoped NCs in each case. Figure 3.11 (Supporting Information) shows the same potentiometric data recast as E_F *vs* equivalents of $FcBF_4$ per NC surface area. These plots show E_F becoming progressively more positive as $FcBF_4$ is added to the

solution of photodoped NCs. At some number of equivalents, E_F drops sharply, indicating that the titration equivalence point has been reached. Beyond the equivalence point, E_F approaches the formal potential of $Fc^{+/0}$ (0 V). These data reflect a redox equilibrium between the NCs and the titrant.

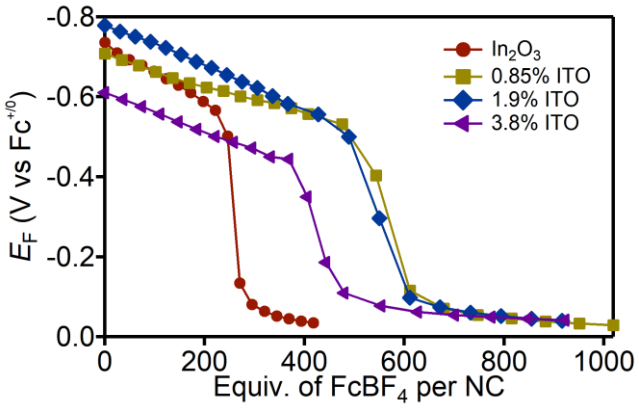

Figure 3.3. Potentiometric titration data for d = 13.1 nm In_2O_3 (red circles), d = 13.4 nm 0.85% ITO (gold squares), d = 14.1 nm 1.9% ITO (blue diamonds), and d = 12.6 nm 3.8% ITO (purple triangles) nanocrystals. The Fermi level (E_F, in V *vs* $Fc^{+/0}$) is plotted against equivalents of $FcBF_4$ per NC added to solutions of maximally photodoped NCs in 0.1 M $TBAPF_6$/THF.

Table 3.1 summarizes the potentiometric data from Fig. 3.3. The slopes of the potentiometric titration curves are given as mV/equiv and provide a measure of the NC redox capacitance (C_r) in this range according to $1/C_r = \Delta V/\Delta Q = m/e$, where m is the titration slope (in V/equiv) and e is the elementary charge. These experimental capacitance values are compared with calculated double layer capacitance values given by Eq. (1), where ϵ_0 is the vacuum permittivity, ϵ = 9 is the dielectric of 0.1 M $TBAPF_6$/THF, r is the NC radius, and t is the double-layer thickness.[24] t is approximated as 2.5 nm, roughly the length of an extended oleate ligand plus a tetrabutylammonium cation.[24] The specific areal capacitance (C_A) is obtained by dividing C_r by the NC surface area.

For ZnO NCs, the experimental C_r is reproduced well by Eq. (1),[24] but for these ITO NCs, the experimental C_r values are an order of magnitude larger than the calculated values. If C_r were due solely to double layer capacitance, the double layer thickness would instead need to be only 1.3–2.0 Å, *e.g.*, only slightly longer than a typical O–H bond (~0.96 Å). Surprisingly, the C_A values measured here are close to those measured in $Fe^{3+/2+}$:ZnO NCs (33 μF cm^{-2}),[26] where the redox activity of the iron dopants provided a substantial boost to the NC capacitance by localizing electrons.

$$C_{dl} = A\frac{\epsilon_0 \epsilon}{r}\frac{r+t}{t} \quad (1)$$

Table 3.1. Experimental redox capacitance (C_r) and areal capacitance (C_A) values, compared with double-layer capacitance (C_{dl}) values calculated from Eq. (1) for In_2O_3 NCs with varying amounts of Sn^{4+} doping.

Sn^{4+} cation %	*m* (mV/equiv)	Experimental C_r (aF)	C_{dl} from Eq. (1) (aF)	C_A (μF cm^{-2})
0	0.71	226	24	41
0.85	0.36	445	25	41
1.9	0.50	302	27	51
3.8	0.47	340	22	65

Because the NIR absorption spectra and E_F were both measured simultaneously as a function of titration with $FcBF_4$ (Figs. 3.2 and 3.3), it is possible to recast the data by plotting one measurement *vs* the other. Figure 3.4 plots E_F values from Fig. 3.3 against the 1300 nm absorption divided by the absorption of the maximally photodoped NCs at the same wavelength (A/A_{max}), from Fig. 3.2. The dashed lines in Fig. 3.4 show linear fits to the data, not including data points in the region of the equivalence point (hollow symbols), and their extrapolation to $A/A_{max} = 0$ provides values of E_F in the limit of no CB electrons (*i.e.*, the CB-edge potential). This plot shows a clear trend of increasingly positive intercept values with increasing Sn^{4+} concentration in the NCs.

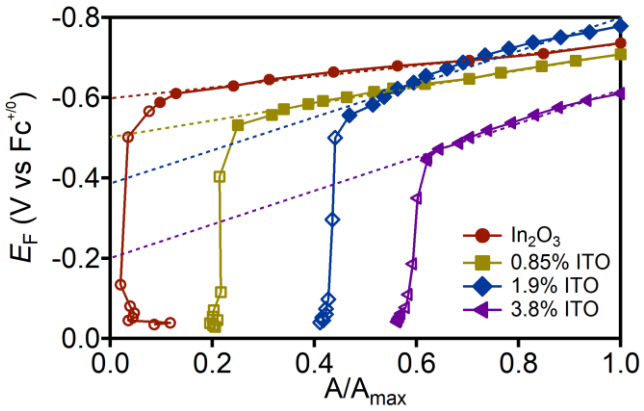

Figure 3.4. Fermi level (E_F, in *V vs* $Fc^{+/0}$) of d = 13.1 nm In_2O_3 (red circles), d = 13.4 nm 0.85% ITO (gold squares), d = 14.1 nm 1.9% ITO (blue diamonds), and d = 12.6 nm 3.8% ITO (purple triangles) NCs, plotted against the absorption at 1300 nm, normalized to the maximum absorption of the fully photodoped NCs (A/A_{max}). The dashed lines are linear fits to the data before the equivalence points, extrapolated to E_F at A/A_{max} = 0. The hollow symbols are data in the region of the equivalence point and are not included in the analysis.

Three important potentials are obtained from the data in Fig. 3.4: the maximum E_F after photodoping ($E_{F\,max}$), the value of E_F at A/A_0 = 1 for the various ITO NC samples ($E_{F\,as\text{-}made}$), and the extrapolated CB-edge potential in the absence of CB electrons (E_{CB}). These values are plotted as a function of Sn^{4+} concentration in Fig. 3.12 (Supporting Information). We note that $E_{F\,as\text{-}made}$ varies from sample to sample because of experimental fluctuations[27] and specific characteristics of the NC surfaces following NC synthesis and workup, such as the specific surface stoichiometries, protonation or other ligation levels, and faceting. To account for these variations, Fig. 3.5a plots these data relative to $E_{F\,as\text{-}made}$. Figure 3.5a shows that maximum photodoping always increases E_F by the roughly same amount (118 ± 20 mV), regardless of NC Sn^{4+} concentration. This observation is consistent with the observation that $\langle N_{photo} \rangle$ is also independent of Sn^{4+} concentration (Fig. 3.10, Supporting Information), and with previously observed Fermi-level pinning in photodoped ZnO NCs.[23] Notably, the data in Fig. 3.5a also show that E_{CB} decreases

by hundreds of mV going from undoped In_2O_3 to 3.8% Sn^{4+}:In_2O_3 NC compositions. These data highlight the conclusion that aliovalent Sn^{4+} dopants *stabilize* the In_2O_3 NC band CB edge, rather than raising the Fermi level into the CB. An average stabilization energy of ~0.55 mV per lattice Sn^{4+} is estimated from these data. The results in Fig. 3.5a are summarized schematically in Fig. 3.5b.

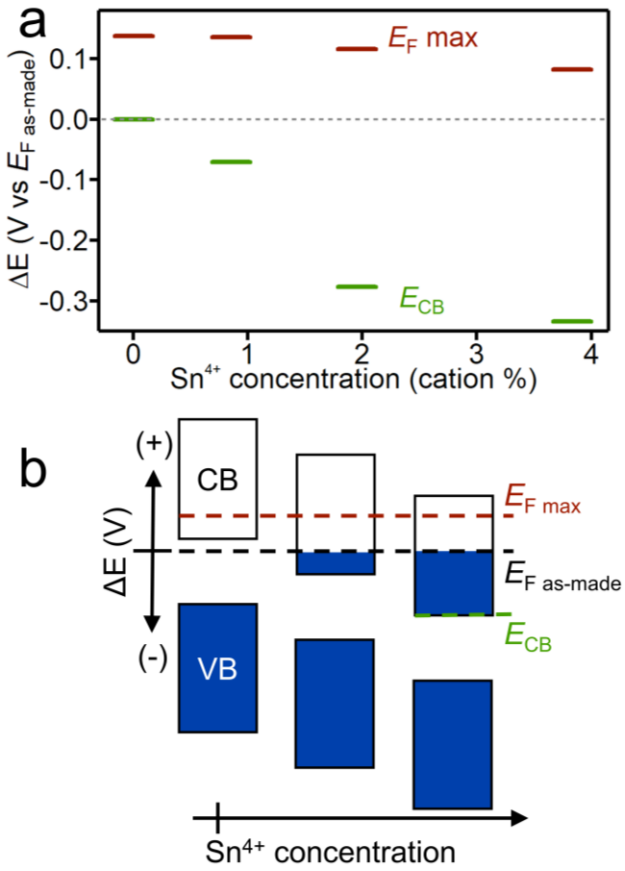

Figure 3.5. (a) Potentials for In_2O_3 NCs doped with different amounts of Sn^{4+}, plotted relative to the potentials measured at $A/A_0 = 1$ ($E_{F\ as\text{-}made}$). The red bars indicate the Fermi levels after maximum photodoping ($E_{F\ max}$). The green bars indicate the CB-edge potentials, derived from extrapolation of the titration data in Fig. 4 to $A/A_{max} = 0$, *i.e.*, in the limit of $\langle n \rangle = 0$. (b) Schematic summary of the results in panel (a), showing band-edge stabilization upon Sn^{4+} doping into In_2O_3 NCs.

Modeling the Electrostatics of Degenerately Doped NCs

To further explore the role of aliovalent dopants on the redox properties of ITO NCs, we employed a hybrid quantum-classical "Charged Sphere" model that quantifies the various electrostatic interactions in these NCs.[25-26] This model has successfully described electrostatics in photodoped ZnO NCs and it has reproduced experimental potentiometric titrations of photodoped ZnO and $Fe^{3+/2+}$:ZnO NCs.[25-26] Here, we expand the model to describe the carrier-stabilization energies that result from the attractive potentials of aliovalent lattice dopants.

We start by qualitatively modeling the potential of the Fermi level electron in degenerately doped NCs that are charge compensated by either aliovalent dopants or surface cations. Figure 3.6 depicts the electrostatic contributions of CB electrons ($q^- = ne$), charge-compensating cations (q^+), and electron affinity (EA) to the total potential ($V(r)$) of the Fermi level electron calculated within this Charged Sphere model for degenerately *n*-doped NCs compensated by either lattice (aliovalent) or surface cations (see Supporting Information for details). V(r) can be interpreted as the potential of a "test" electron interacting with a NC containing q^- (electron) and q^+ (cation) charges. Figure 3.6a qualitatively shows that $V(r)$ is stabilized (E_F decreases) in the core of the NC when the charge-compensating cations are distributed isotropically within the NC lattice as aliovalent dopants. Meanwhile, surface charge-compensating cations such as H^+ or electrolyte in a capacitive charging experiment minimize $V(r)$ near the NC surfaces rather than in the NC core (Fig. 3.6b). In both scenarios, the CB electrons are delocalized over large volumes, but these potential-energy surfaces determine the electron density distribution and E_F for any given combination of q^- and q^+.[25]

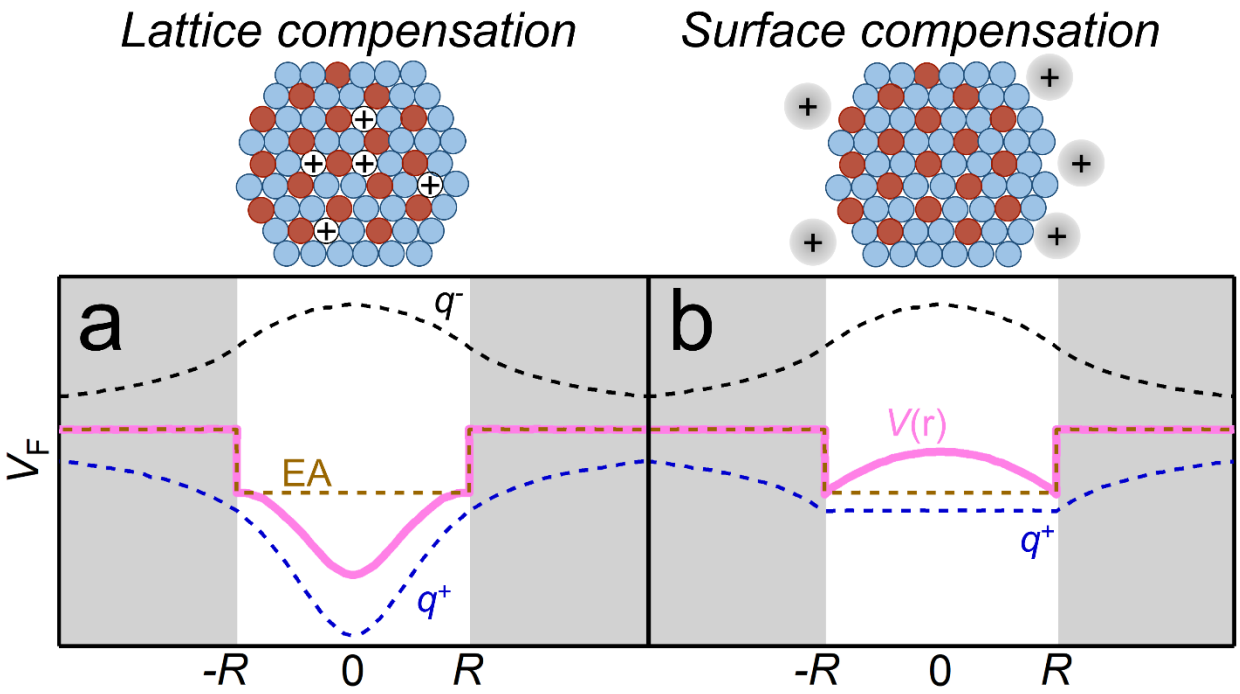

Figure 3.6. Schematic illustration of electron potentials for degenerately *n*-doped NCs compensated by either lattice (a) or surface cations (b), as described by the Charged Sphere model. Potentials are plotted as a function of distance from the center of the NC, where the white region represents the NC interior, *R* represents the NC radius (surface), and the shaded region represents the NC's dielectric surrounding. Electrostatic contributions from CB electrons (q^-, black), charge-compensating cations (q^+, blue), and electron affinity (EA, gold) combine to define the total potential, *V*(*r*) (pink). Above the panels are schematic representations of *n*-doped NCs with electron charges compensated by lattice (a) or surface (b) cations. Both panels were calculated for values of $q^- = q^+ = 20$ and $R = 6.25$ nm.

Further theoretical modeling is ongoing as part of a collaborative effort with Professor Xiaosong Li's group at the University of Washington. First, we will use the calculated *V*(r) to quantitatively reproduce the experimental CB stabilization energy (Supporting Information). Initial results show that *V*(*r*) becomes increasingly stabilized as more q^+/q^- are added to the model, assuming a uniform distribution of q^+. Further optimization of the radial density function may improve agreement with experimental data. The observation that only ~ 46% of Sn^{4+} dopants stabilize electrons in the ITO nanocrystal CB (from Fig. 3.2b, 1.9% ITO NCs) suggests that aliovalent dopants at or near the NC surface do not stabilize CB electrons, as seen in previous reports of AZO[8-9] and ITO NCs.[10] Therefore, a gradient in q^+ or in the electrostatic contribution of

each aliovalent dopant may be necessary to accurately reproduce experimental CB stabilization energies.

Additionally, we will explore the wavefunction of the Fermi-level electron as a function of aliovalent doping. Previous modeling on degenerately doped ZnO NCs showed that Coulombic repulsion expands the radial wavefunction towards the NC surface as q^- increases.[25] Aliovalent dopants may screen these repulsive interactions, stabilizing the wavefunction in the NC core, even at high electron densities. Finally, we will simulate titration data for these ITO NCs. Titration data were simulated for $Fe^{3+/2+}$:ZnO NCs,[26] but in this case the iron dopants were redox active, resulting in partial localization of electrons and no CB stabilization. Potentiometric titration simulations of ITO NCs will also reveal the effect of Coulombic repulsion between surface cations on the NC capacitance.

3.4 **Discussion**

The results presented above highlight the important role of aliovalent dopants in determining the band-edge potentials of ITO NCs. Spectroelectrochemical data show stabilization of the CB edge by ~0.55 mV per lattice Sn^{4+}. Similarly, the "Charged Sphere" electrostatic model predicts stabilization of the ITO NC CB with increasing concentration of aliovalent dopants. Further quantitative modeling is forthcoming.

The experimental CB stabilization energy in ITO NCs is smaller than that found in *p*-doped d = 5.4 nm $Cu_{2-x}S$ NCs,[27] where each Cu^+ vacancy stabilizes a valence-band hole by ~2.3 mV (determined at a hole density ~ 1.5×10^{21} cm^{-3}). Nevertheless, the band stabilization per aliovalent lattice dopant is similar in magnitude, even though the NC structure, composition, and excess charge-carrier type are all different. These observations support the conclusion of band stabilization in aliovalently doped NCs being determined by electrostatics.

The spectroelectrochemical data also draw sharp attention to the difference between CB electrons added *via* aliovalent doping (CB stabilization) and *via* photodoping (Fermi level raising): all e^-_{photo} can be removed by the mild oxidant $FcBF_4$ (0.3–0.7 mV/e^-_{photo}), but only ~30% of e^-_{alio} can be removed using the same oxidant. Similar trends are observed in other aliovalently doped NCs.[8,10] This difference reflects the importance of the specific charge-compensating motif in determining the reactivity of the CB electron. In the case of e^-_{photo}, charge-compensating surface protons can assist in discharging the NC through proton-coupled electron transfer (PCET),[30-31] or can merely provide less stabilization of e^-_{photo} because of its spatial separation,[23-25] whereas e^-_{alio} are stabilized more effectively by aliovalent dopants, and removal of these electrons is energetically more costly because it requires separating charges.[8]

Finally, we note that the capacitance values measured in these In_2O_3-based NCs (C_r = 220–240 aF, C_A = 40–65 μF cm^{-2}) are surprisingly large compared to values measured for analogous ZnO NCs (C_r = 2–12 aF, C_A = 4 μF cm^{-2}) and even compared to $Fe^{3+/2+}$:ZnO NCs (C_r = 45–80 aF, C_A = 33 μF cm).[24,26] The density of states is calculated to be smaller at CB-edge of In_2O_3 compared to higher in the band,[32] and there is noticeable size and morphology distribution in these NCs, ruling out this difference coming from quantum capacitance.[24] Partial reduction of Sn^{4+} could conceivably lead to increased pseudocapacitance, but even the undoped In_2O_3 NCs show a large capacitance (226 aF, 41 μF cm^{-2}). Alternatively, the large capacitance could be an effect of the NC size dependence of surface Coulomb interactions. For example, a NC with r = 2.5 nm and a carrier density of $\langle N_{photo} \rangle$ = 1.5 × 10^{20} cm^{-3} would require 0.1 H^+/nm^2 at its surface for charge compensation, whereas a NC with r = 6.1 nm and the same carrier density would require 0.3 H^+/nm^2. The increase in surface H^+–H^+ Coulomb repulsion resulting from this increase in H^+

density will allow electrons to be removed more easily in order to reduce this repulsion, *i.e.*, will increase the NC capacitance. This effect will be further explored by theoretical modeling.

3.5 **Summary**

The impact of carrier-charge compensation in degenerately doped oxide NCs has been examined both experimentally and computationally. Using ITO NCs as a model system, the potentials of CB electrons added *via* photodoping were measured quantitatively as a function of the number of added CB electrons. Analysis of these data shows that the CB is dramatically stabilized by incorporation of Sn^{4+} dopants into the In_2O_3 NC lattice. A marked difference is observed between the potentials of delocalized CB electrons compensated by aliovalent dopants and those compensated by surface cations (*e.g.*, H^+). Theoretical modeling confirms that aliovalent dopants stabilize the CB potential deep within the NC core, in contrast with surface-cation compensation, which leads to a CB potential minimum close to the NC surface. These results represent a case study of electrostatics and band-edge stabilization trends that are anticipated to apply broadly among aliovalently doped NCs as a class, and as such they inform the use of such plasmonic semiconductor NCs in optoelectronic technologies.

3.6 **Experimental**

3.6.1 *ITO Nanocrystal Synthesis.*

In_2O_3 and ITO NCs were synthesized according to previously published procedures.[6,15] Briefly, 7.5 mmol of metal acetate were added to a 100 mL three-neck flask along with 15 mL of OA. Tin doping was achieved by holding the total metal content at 7.5 mmol and adjusting the ration of Sn:In. The solution was then heated with stirring under N_2 with a purge needle for at least

2 h to obtain a 0.5 mmol/mL solution. 13 mL of oleyl alcohol were added to a separate 100 mL three-neck flask that was fitted with three septa. Three 16-gauge needles were added to one side, and a 16-gauge needle was added to the other side with a N_2 flow of 130 cc/min. The flask was then heated to 290 °C. Next, 10 mL of the ITO precursor solution was injected using a glass syringe and syringe pump at a rate of 0.35 mL/min. The flask was then allowed to cool to room temperature, and the NCs were collected by precipitation with EtOH and centrifugation. The product was then suspended in toluene and precipitated with EtOH. This washing procedure was repeated three more times. Finally, the NCs were dispersed in hexanes and filtered with a 0.2 μm PTFE syringe filter. The solvent was then evaporated, and the product pumped into a N_2 glovebox. The NCs were dispersed in anhydrous THF for further analysis.

3.6.2 *Physical Measurements.*

All UV-vis-NIR absorption spectra were collected at room temperature using a Cary 5000 spectrophotometer (Agilent) and fiber-optic coupling into a N_2 glovebox. Transmission electron microscope (TEM) images were taken on a FEI Tecnai G2 F20 operating at 200 kV. NC concentrations were determined using a combination of TEM and inductively coupled plasma atomic emission spectroscopy (ICP-AES, Perkin Elmer) of dried NCs digested in ultrapure nitric acid.

3.6.3 *Photodoping and Spectroelectrochemistry.*

All electrochemical measurements were performed in a N_2 glovebox with a Gamry potentiostat under galvanostatic control with $I = 0$ A. Two Pt wires were used for the working and counter electrode, and a 1-mm leakless Ag/AgCl electrode (eDAQ) was used as a reference. The

electrodes were fitted through the septum of a GL-14 cap and secured on a 1-cm quartz cuvette containing 3.5 mL of 0.1 M $TBAPF_6$/THF, 10 μL of anhydrous EtOH, and 15-50 μL of NC solution. The solution was magnetically stirred during the experiment. The absorption spectrum was collected and the open-circuit potential (V_{OC}) was allowed to equilibrate, then the solution was irradiated with a 340 nm LED to allow the NCs to maximally photodope. Because of small excitation rates, maximum photodoping required several hours (5–8 h) illumination under these conditions. $FcBF_4$ was dissolved in 0.1 M $TBAPF_6$/THF and this solution was further diluted in fresh 0.1 M $TBAPF_6$/THF such that 5 μL of the dilute solution contained 15-35 equivalents of Fc^+ per NC. After allowing the NCs to maximally photodope, the absorption spectrum was measured, and then an aliquot of $FcBF_4$ was injected through the septum. The V_{OC} was allowed to equilibrate, and the absorption spectrum was measured again. Potentials and absorption data were thus measured simultaneously. This injection/equilibration/measurement cycle was repeated until a large excess of $FcBF_4$ had been added, as judged from V_{OC}. All potentials were referenced to the $E_{1/2}$ of $Fc^{+/0}$ measured by cyclic voltammetry following the potentiometry measurements.

3.6.4 *Theoretical modeling.*

The previously reported quantum-classical model was adapted to simulate the Fermi levels of doped NCs.[25-26] The effect of existing CB electrons (e_{CB}^-) and uncompensated interior cations are approximated as a mean-field potential (V(r)) in the Hamiltonian, as described by Eq (2).

$$\mathrm{H} = \frac{1}{2}\frac{d^2}{dr^2} + \frac{l(l+1)}{2r^2} + V(r) \qquad (2)$$

The mean-field potential can be derived from Gauss's law using Eq. (3) and (4) as stated previously.[25-26] The density radial distribution, ρ(r), of the e_{CB}^- and uncompensated cations is

simplified using the uniform charge distribution. The details of calculating the Fermi level can be found in the Supporting Information.

$$\mathrm{V(r)} = \int_{\infty}^{r} E(r')dr' \tag{3}$$

$$E(r) = \frac{\iiint \rho(r)dV}{r^2} \tag{4}$$

3.7 **References**

1. Schimpf, A. M.; Knowles, K. E.; Carroll, G. M.; Gamelin, D. R., Electronic doping and redox-potential tuning in colloidal semiconductor nanocrystals. *Acc. Chem. Res.* **2015,** *48*, 1929-37.
2. Araujo, J. J.; Brozek, C. K.; Kroupa, D. M.; Gamelin, D. R., Degenerately n-Doped Colloidal PbSe Quantum Dots: Band Assignments and Electrostatic Effects. *Nano Lett.* **2018,** *18*, 3893-3900.
3. Staller, C. M.; Gibbs, S. L.; Saez Cabezas, C. A.; Milliron, D. J., Quantitative Analysis of Extinction Coefficients of Tin-Doped Indium Oxide Nanocrystal Ensembles. *Nano Lett.* **2019,** *19*, 8149-8154.
4. Agrawal, A.; Cho, S. H.; Zandi, O.; Ghosh, S.; Johns, R. W.; Milliron, D. J., Localized Surface Plasmon Resonance in Semiconductor Nanocrystals. *Chem. Rev.* **2018,** *118*, 3121-3207.
5. Luther, J. M.; Jain, P. K.; Ewers, T.; Alivisatos, A. P., Localized surface plasmon resonances arising from free carriers in doped quantum dots. *Nat. Mater.* **2011,** *10*, 361-6.
6. Crockett, B. M.; Jansons, A. W.; Koskela, K. M.; Johnson, D. W.; Hutchison, J. E., Radial Dopant Placement for Tuning Plasmonic Properties in Metal Oxide Nanocrystals. *ACS Nano* **2017,** *11*, 7719-7728.
7. Kriegel, I.; Scotognella, F.; Manna, L., Plasmonic doped semiconductor nanocrystals: Properties, fabrication, applications and perspectives. *Phys. Rep.* **2017,** *674*, 1-52.
8. Schimpf, A. M.; Ochsenbein, S. T.; Buonsanti, R.; Milliron, D. J.; Gamelin, D. R., Comparison of extra electrons in colloidal n-type Al(3+)-doped and photochemically reduced ZnO nanocrystals. *Chem. Commun.* **2012,** *48*, 9352-4.
9. Zhou, D.; Wang, P.; Roy, C. R.; Barnes, M. D.; Kittilstved, K. R., Direct Evidence of Surface Charges in n-Type Al-Doped ZnO. *J. Phys. Chem. C* **2018,** *122*, 18596-18602.
10. Schimpf, A. M.; Lounis, S. D.; Runnerstrom, E. L.; Milliron, D. J.; Gamelin, D. R., Redox chemistries and plasmon energies of photodoped In_2O_3 and Sn-doped In_2O_3 (ITO) nanocrystals. *J. Am. Chem. Soc.* **2015,** *137*, 518-24.
11. Crockett, B. M.; Jansons, A. W.; Koskela, K. M.; Sharps, M. C.; Johnson, D. W.; Hutchison, J. E., Influence of Nanocrystal Size on the Optoelectronic Properties of Thin, Solution-Cast Sn-Doped In2O3 Films. *Chem. Mater.* **2019,** *31*, 3370-3380.
12. Gordon, T. R.; Paik, T.; Klein, D. R.; Naik, G. V.; Caglayan, H.; Boltasseva, A.; Murray, C. B., Shape-dependent plasmonic response and directed self-assembly in a new semiconductor building block, indium-doped cadmium oxide (ICO). *Nano Lett.* **2013,** *13*, 2857-63.
13. Kriegel, I.; Urso, C.; Viola, D.; De Trizio, L.; Scotognella, F.; Cerullo, G.; Manna, L., Ultrafast Photodoping and Plasmon Dynamics in Fluorine-Indium Codoped Cadmium Oxide Nanocrystals for All-Optical Signal Manipulation at Optical Communication Wavelengths. *J. Phys. Chem. Lett.* **2016,** *7*, 3873-3881.
14. Runnerstrom, E. L.; Llordes, A.; Lounis, S. D.; Milliron, D. J., Nanostructured electrochromic smart windows: traditional materials and NIR-selective plasmonic nanocrystals. *Chem. Commun.* **2014,** *50*, 10555-72.
15. Jansons, A. W.; Hutchison, J. E., Continuous Growth of Metal Oxide Nanocrystals: Enhanced Control of Nanocrystal Size and Radial Dopant Distribution. *ACS Nano* **2016,** *10*, 6942-51.

16. Agrawal, A.; Kriegel, I.; Runnerstrom, E. L.; Scotognella, F.; Llordes, A.; Milliron, D. J., Rationalizing the Impact of Surface Depletion on Electrochemical Modulation of Plasmon Resonance Absorption in Metal Oxide Nanocrystals. *ACS Photonics* **2018,** *5*, 2044-2050.
17. Zandi, O.; Agrawal, A.; Shearer, A. B.; Reimnitz, L. C.; Dahlman, C. J.; Staller, C. M.; Milliron, D. J., Impacts of surface depletion on the plasmonic properties of doped semiconductor nanocrystals. *Nat. Mater.* **2018,** *17*, 710-717.
18. Schimpf, A. M.; Gunthardt, C. E.; Rinehart, J. D.; Mayer, J. M.; Gamelin, D. R., Controlling carrier densities in photochemically reduced colloidal ZnO nanocrystals: size dependence and role of the hole quencher. *J. Am. Chem. Soc.* **2013,** *135*, 16569-77.
19. Valdez, C. N.; Braten, M.; Soria, A.; Gamelin, D. R.; Mayer, J. M., Effect of protons on the redox chemistry of colloidal zinc oxide nanocrystals. *J. Am. Chem. Soc.* **2013,** *135*, 8492-5.
20. Valdez, C. N.; Delley, M. F.; Mayer, J. M., Cation Effects on the Reduction of Colloidal ZnO Nanocrystals. *J. Am. Chem. Soc.* **2018,** *140*, 8924-8933.
21. Valdez, C. N.; Schimpf, A. M.; Gamelin, D. R.; Mayer, J. M., Proton-Controlled Reduction of ZnO Nanocrystals: Effects of Molecular Reductants, Cations, and Thermodynamic Limitations. *J. Am. Chem. Soc.* **2016,** *138*, 1377-85.
22. Goings, J. J.; Schimpf, A. M.; May, J. W.; Johns, R. W.; Gamelin, D. R.; Li, X., Theoretical Characterization of Conduction-Band Electrons in Photodoped and Aluminum-Doped Zinc Oxide (AZO) Quantum Dots. *J. Phys. Chem. C* **2014,** *118*, 26584-26590.
23. Carroll, G. M.; Schimpf, A. M.; Tsui, E. Y.; Gamelin, D. R., Redox Potentials of Colloidal n-Type ZnO Nanocrystals: Effects of Confinement, Electron Density, and Fermi-Level Pinning by Aldehyde Hydrogenation. *J. Am. Chem. Soc.* **2015,** *137*, 11163-9.
24. Brozek, C. K.; Hartstein, K. H.; Gamelin, D. R., Potentiometric Titrations for Measuring the Capacitance of Colloidal Photodoped ZnO Nanocrystals. *J. Am. Chem. Soc.* **2016,** *138*, 10605-10.
25. Liu, H.; Brozek, C. K.; Sun, S.; Lingerfelt, D. B.; Gamelin, D. R.; Li, X., A Hybrid Quantum-Classical Model of Electrostatics in Multiply Charged Quantum Dots. *J. Phys. Chem. C* **2017,** *121*, 26086-26095.
26. Brozek, C. K.; Zhou, D.; Liu, H.; Li, X.; Kittilstved, K. R.; Gamelin, D. R., Soluble Supercapacitors: Large and Reversible Charge Storage in Colloidal Iron-Doped ZnO Nanocrystals. *Nano Lett.* **2018,** *18*, 3297-3302.
27. Hartstein, K. H.; Brozek, C. K.; Hinterding, S. O. M.; Gamelin, D. R., Copper-Coupled Electron Transfer in Colloidal Plasmonic Copper-Sulfide Nanocrystals Probed by in Situ Spectroelectrochemistry. *J. Am. Chem. Soc.* **2018,** *140*, 3434-3442.
28. Farvid, S. S.; Hegde, M.; Radovanovic, P. V., Influence of the Host Lattice Electronic Structure on Dilute Magnetic Interactions in Polymorphic Cr(III)-Doped In2O3 Nanocrystals. *Chem. Mater.* **2013,** *25*, 233-244.
29. Farvid, S. S.; Ju, L.; Worden, M.; Radovanovic, P. V., Colloidal Chromium-Doped In2O3 Nanocrystals as Building Blocks for High-TC Ferromagnetic Transparent Conducting Oxide Structures. *J. Phys. Chem. C* **2008,** *112*, 17755-17759.
30. Schrauben, J. N.; Hayoun, R.; Valdez, C. N.; Braten, M.; Fridley, L.; Mayer, J. M., Titanium and zinc oxide nanoparticles are proton-coupled electron transfer agents. *Science* **2012,** *336*, 1298-301.
31. Braten, M. N.; Gamelin, D. R.; Mayer, J. M., Reaction Dynamics of Proton-Coupled Electron Transfer from Reduced ZnO Nanocrystals. *ACS Nano* **2015,** *9*, 10258-67.

32. Chen, Z.; Huang, L.; Zhang, Q.; Xi, Y.; Li, R.; Li, W.; Xu, G.; Cheng, H., Electronic Structures and Transport Properties of n-Type-Doped Indium Oxides. *J. Phys. Chem. C* **2015,** *119*, 4789-4795.

3.8 **Supporting Information**

3.8.1 *Spectroelectrochemical data*

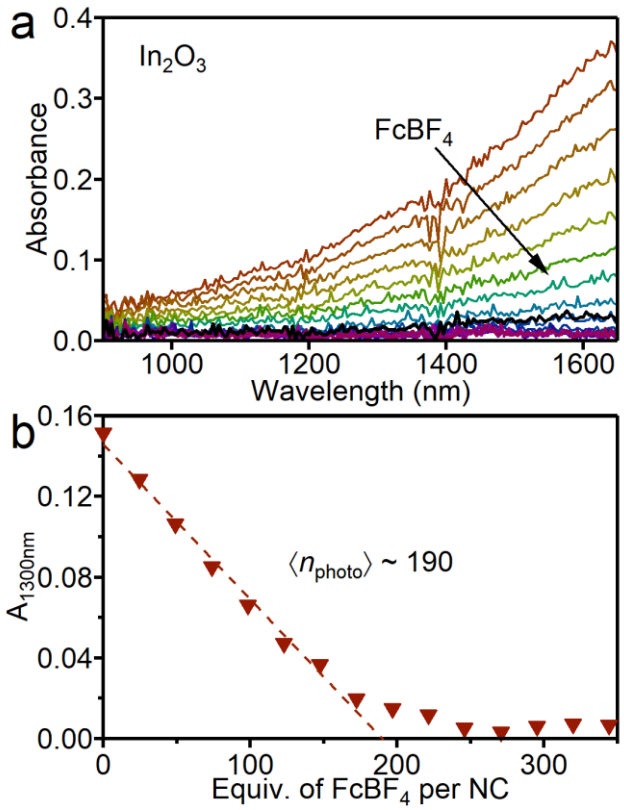

Figure 3.7. (a) Absorption spectra of a solution of maximally photodoped d = 13.1 nm In_2O_3 NCs, collected at various stages during oxidative titration with $FcBF_4$. The NCs were suspended in in 0.1 M $TBAPF_6$/THF. The arrow shows the direction of increasing oxidative equivalents. The black spectrum is the absorption of the as-prepared solution. (b) Absorbance at 1300 nm plotted against equivalents of $FcBF_4$ added to the maximally photodoped NCs from panel (a). The dashed red line is a fit to the data for values less than 150.

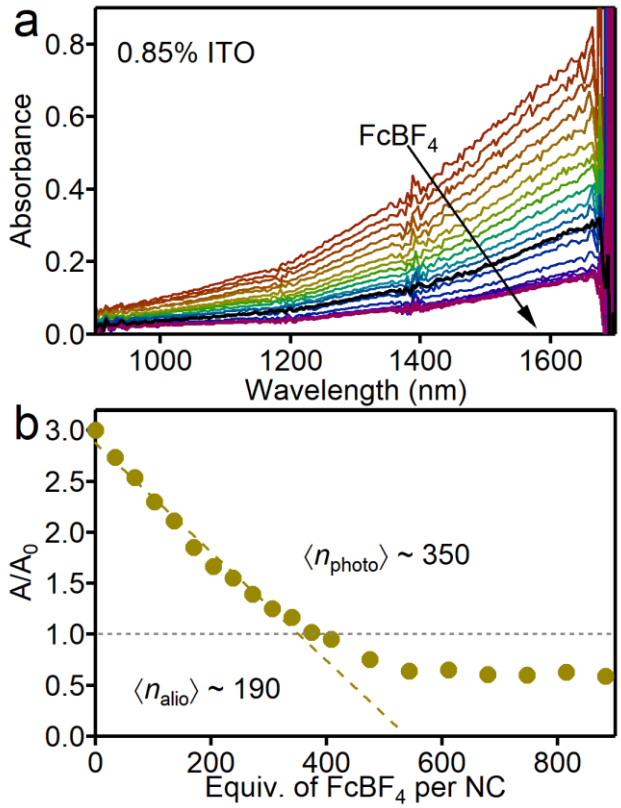

Figure 3.8. (a) Absorption spectra of a solution of maximally photodoped d = 13.4 nm ITO NCs containing 0.85% Sn^{4+}, collected at various stages during oxidative titration with $FcBF_4$. The NCs were suspended in in 0.1 M $TBAPF_6$/THF. The arrow shows the direction of increasing oxidative equivalents. The black spectrum is the absorption of the as-prepared solution. (b) The ratio of the absorbance at 1300 nm to the absorbance of the as-prepared solution at the same wavelength (A/A_0), plotted against equivalents of $FcBF_4$ added to the maximally photodoped NCs from panel (a). The gray dashed line at A/A_0 = 1 represents the absorption of the as-prepared solution. The dashed gold line is a fit to the data for values of A/A_0 greater than 1 and is extrapolated to A/A_0 = 0.

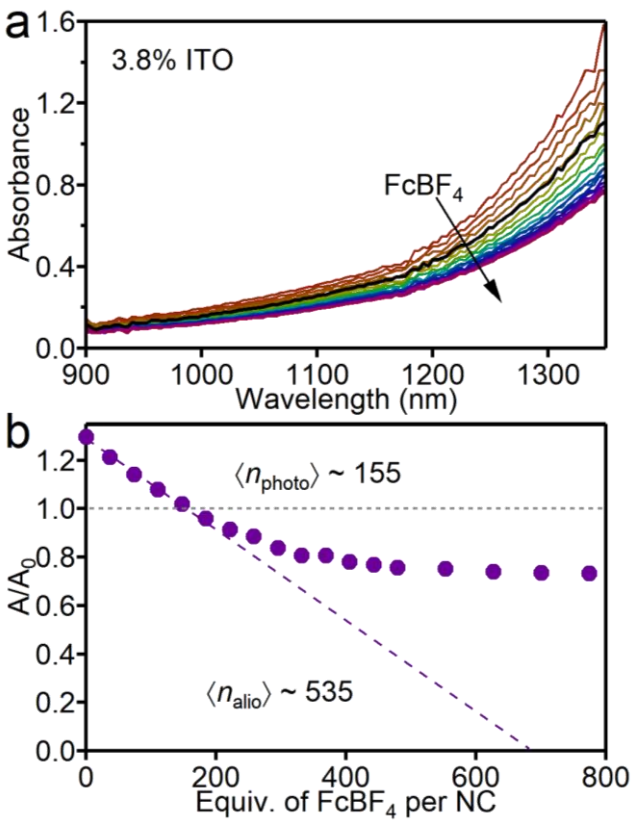

Figure 3.9. (a) Absorption spectra of a solution of maximally photodoped d = 12.6 nm ITO NCs containing 3.8% Sn^{4+}, collected at various stages during oxidative titration with $FcBF_4$. The NCs were suspended in in 0.1 M $TBAPF_6$/THF. The arrow shows the direction of increasing oxidative equivalents. The black spectrum is the absorption of the as-prepared solution. (b) The ratio of the absorbance at 1300 nm to the absorbance of the as-prepared solution at the same wavelength (A/A_0), plotted against equivalents of $FcBF_4$ added to the maximally photodoped NCs from panel (a). The gray dashed line at A/A_0 = 1 represents the absorption of the as-prepared solution. The dashed purple line is a fit to the data for values of A/A_0 greater than 1 and is extrapolated to A/A_0 = 0.

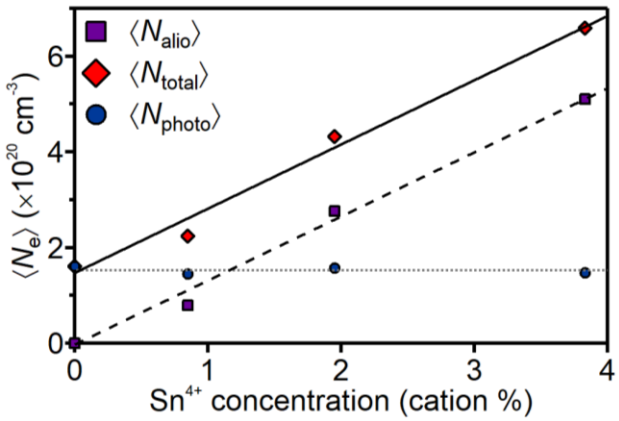

Figure 3.10. Electron density (× 10^{20} cm^{-3}) for electrons compensated by aliovalent dopants (purple squares), electrons added by photodoping (blue circles), and total electron density (red diamonds). The dotted gray line at ~ 1.5 × 10^{20} cm^{-3} is a guide to the eye highlighting a constant value of $\langle N_{photo} \rangle$ across the range of Sn^{4+} concentrations. The diagonal dashed line is a guide to the eye showing increasing $\langle N_{alio} \rangle$ with increasing Sn^{4+} concentration, and the solid diagonal line is a guide to the eye showing the total electron density of the maximally photodoped NCs ($\langle N_{total} \rangle = \langle N_{alio} \rangle + \langle N_{photo} \rangle$).

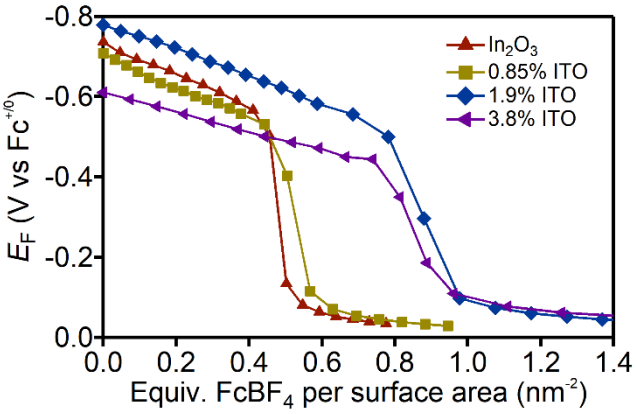

Figure 3.11. Potentiometric titration data for d = 13.1 nm In_2O_3 (red triangles), d = 13.4 nm 0.85% ITO (gold triangles), d = 14.1 nm 1.9% ITO (blue triangles), and d = 12.6 nm 3.8% ITO (purple triangles) nanocrystals. The Fermi level (E_F, in V *vs* $Fc^{+/0}$) is plotted against equivalents of $FcBF_4$ per unit surface area (nm^2) added to solutions of maximally photodoped NCs in 0.1 M $TBAPF_6$/THF.

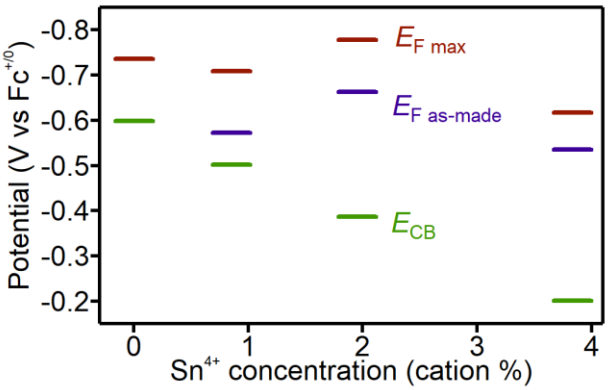

Figure 3.12. Potentials for In_2O_3 NCs with varying Sn^{4+} content. The red bars indicate the maximum Fermi levels after maximum photodoping. The purple bars indicate the potentials at $A/A_0 = 1$ for the ITO samples. The green bars indicate the CB-edge potentials, derived from extrapolation of the data in Figure 3.4 to the Fermi level at $A/A_{max} = 0$.

3.8.2 *Computational Methods*

Hybrid Quantum-Classical "Charged Sphere" Model. All calculations employ a modified version of the hybrid quantum-classical "Charged Sphere" model described previously.[1-2] In short, the energetics of e_{CB}^- within *n*-type spherical QDs are computed quantum mechanically by treating e_{CB}^- as particles in a finite potential that is classically determined. We first determine the potential $V(r)$ acting on a single-particle wavefunction $\psi(r)$. Using Gauss's law, electron-electron/hole-hole repulsion and electron-cation/hole-anion stabilization are approximated as a mean-field potential. The electron-electron exchange energies are neglected in the model due to their minor contribution to the orbital energies. As a cross-check, we performed an analytical integration of s-p repulsion and s-p exchange on d = 4~10 nm spheres using an infinite square potential well (analytical integration is not feasible for a finite well) and found that in all cases the exchange energies are an order of magnitude smaller than repulsions. Therefore, neglecting exchange slightly increases orbital energies, but retains the qualitative result.

As a starting point, e_{CB}^{-} are initially treated as uniformly distributed, whereas surface charge-compensating cations are always treated as an evenly distributed charge shell. Overall, the quantum dots maintain charge neutrality.

For a specific configuration of spatially distributed and negatively charged particles, we use Gauss's law to calculate $V(r)$ in the Hamiltonian as shown in Eq. S2 from the corresponding electric field,

$$\hat{\mathrm{H}} = \frac{1}{2}\frac{d^2}{dr^2} + \frac{l(l+1)}{2r^2} + V(r) \tag{S2}$$

For charged particles, Gauss's law can be written as

$$\oiint \vec{D} \cdot d\vec{S} = \iiint \rho dV \tag{S3}$$

The left-hand side integrates the electric displacement field over the surface area of an arbitrary Gauss's sphere, and the right-hand side gives the total number of effective charges included in the sphere.

Assuming we only draw Gauss's sphere inside the QD, Eq. S3 can be expanded as:

$$\epsilon_0 \epsilon E(r) 4\pi \mathrm{r}^2 = \iiint \rho dV \tag{S4}$$

Initially, particle density ρ on the right-hand side of Eq. S4 is treated as a uniform distribution across the QD sphere independent of r. Therefore, $E(r)$ becomes:

$$E(r) = \frac{Q}{\frac{4}{3}\pi R^3} \times \frac{\frac{4}{3}\pi r^3}{4\pi\epsilon_0 \epsilon r^2} \tag{S5}$$

The potential at a distance *r* is easily determined by integration:

$$V(r) = \int_{\infty}^{r} E(r')dr' \tag{S6}$$

The same treatment can be applied to derive the potential outside the QD. If the potential $V(r)$ is determined electrostatically, then it should be a continuous function spanning the radial coordinate. In the model, we introduce quantum effects in the form of electron affinity (*EA*) for the e_{CB}^{-} to further confine the particles from escaping the dots. Therefore, the overall potential *V(r)* is a piece-wise function:

$$V_{tot}(r) = \begin{cases} V_{in}(r) - EA, & r < R \\ V_{out}(r), & r \geq R \end{cases} \quad \text{(S7)}$$

Substituting $V_{tot}(r)$ back into Eq. S2 gives the Hamiltonian for calculating the orbital energy (eigenvalue) and wavefunction $\psi(r)$ (eigenvector) of the Fermi electron in the QD through simple numerical methods.

To improve accuracy, iterative calculations can be performed by using the computed $\psi(r)^2$ to define $\rho(r)$ as a starting point for ρ in Eq. S4. For iterative calculations, the right-hand side needs to be integrated from $0 \rightarrow r$ before moving the $4\pi\epsilon_0\epsilon r^2$ term to its denominator:

$$E(r) = \frac{\int_0^r 4\pi r'^2 \rho(r') dr'}{4\pi\epsilon_0\epsilon r^2} \quad \text{(S8)}$$

Improved $E(r)$ can be calculated through repeated iterations, but to balance accuracy and computational cost we employ only one additional iteration.

In the model, the electron affinity and dielectric constant of the material and the dielectric constant of the solvent are required as input parameters. For all calculations, the dielectric constant of the solvent (0.1 M $TBAPF_6$/THF) is 9.0. The dielectric constant and *E*A of ITO is chosen to be the same as pure In_2O_3, *i.e.*, ε_0 = 12.5 and *EA* = 4.1 eV. The Fermi-level of electronically doped ITO nanocrystals is obtained by solving the 1D radial Schrodinger equations.

References.

1. Liu, H.; Brozek, C. K.; Sun, S.; Lingerfelt, D. B.; Gamelin, D. R.; Li, X., A Hybrid Quantum-Classical Model of Electrostatics in Multiply Charged Quantum Dots. *J. Phys. Chem. C* **2017,** *121*, 26086-26095.
2. Brozek, C. K.; Zhou, D.; Liu, H.; Li, X.; Kittilstved, K. R.; Gamelin, D. R., Soluble Supercapacitors: Large and Reversible Charge Storage in Colloidal Iron-Doped ZnO Nanocrystals. *Nano Lett.* **2018,** *18*, 3297-3302.